

# Atmospheric icing in a changing climate

*Impact of higher boundary temperatures  
on simulations of atmospheric ice  
accretion on structures during the  
2015-2016 icing winter in West-Norway*

Kristian Ingvaldsen



Thesis submitted for the degree of  
Master in Geosciences  
60 credits

Department of Geosciences  
Faculty of mathematics and natural sciences

UNIVERSITY OF OSLO

Spring 2017



# **Atmospheric icing in a changing climate**

*Impact of higher boundary temperatures  
on simulations of atmospheric ice  
accretion on structures during the  
2015-2016 icing winter in West-Norway*





© 2017 Kristian Ingvaldsen

Atmospheric icing in a changing climate

<http://www.duo.uio.no/>

Printed: Reprosentralen, University of Oslo

## Abstract

Atmospheric icing has been studied for several decades, not only due to the hazardous consequences it can have to air traffic, but also due to the damage it can cause to human installations such as power lines, wind turbines and radio towers etc. Overhead structures that are built in mountainous regions at mid- and high latitudes are particularly vulnerable to the exposure of supercooled water in clouds. The aim of this study is to quantify the possible effects that increased, global temperatures may have on atmospheric icing conditions in the complex orography of western Norway.

Using the Weather Research and Forecasting (WRF) Model we did two simulations of the full 2015-16 winter season covering approximately 18000  $km^2$  of the mountainous regions of western Norway. The model was forced by ERA-Interim reanalysis data, and applied the Thompson microphysics scheme. The first simulation was used as a control run. Calculations of accumulated ice loads on a so-called standard icing object based on the output from this simulation were compared to observations provided by state-of-the-art instruments. The second simulation was made using modified input data, where initial- and boundary temperatures of the model were increased by 2 °C while the relative humidity was kept the same, allowing for higher specific humidity. The results showed significantly smaller accumulative ice loads in the warm run compared to the control. This was found to be mostly due to several episodes where the temperature was above freezing in the warm run and just below freezing in the control run, resulting in fewer icing events as well as more frequent melting episodes in the warm run. The differences seemed to increase with terrain height, and only sporadic events where the icing intensity was higher in the warm run were found. The differences in frequency and intensity of atmospheric icing can be partially explained by a spatial redistribution of high atmospheric water content in the warm run compared to the control run.



## *Acknowledgements*

I would like to sincerely thank my supervisors Terje Koren Berntsen, Hálf dán Ágústsson and Bjørn Egil Nygaard for helpful guidance and contributions during the entire process of this thesis. I would also like to express my gratitude to Kjeller Vindteknikk and all its staff members for providing me with software, data, technical support and a pleasant working environment. Thanks also to Åsmund Bakketun for helpful ideas and valuable discussions, and to Vida Saure for proofreading and continuous support during the entire process.

A special thanks to my former supervisor, Jón Egill Kristjánsson, who sadly passed away in the early stages of this project. It was him who first got me interested in the subject of atmospheric icing.



<b>Abstract</b>	<b>i</b>
<b>Acknowledgements</b>	<b>iii</b>
<b>1 Introduction</b>	<b>1</b>
1.1 What is atmospheric icing?	1
1.2 Atmospheric icing in a changing climate	2
1.3 Thesis overview	4
<b>2 Theory</b>	<b>5</b>
2.1 How do icing events occur?	5
2.1.1 In-cloud icing	5
2.1.2 Freezing rain/drizzle and wet snow accretion	6
2.1.3 Dry growth vs. wet growth	7
2.2 Models of ice growth on structures	7
2.2.1 Growth rate of ice on a standard icing object	8
Collision efficiency, $\alpha_1$	9
Sticking efficiency, $\alpha_2$	9
Accretion efficiency, $\alpha_3$	10
Icing rate	10
2.3 Increased temperature and the impact on humidity conditions	11
<b>3 Methods</b>	<b>13</b>
3.1 Model setup	13
3.1.1 Cloud microphysics scheme	14
3.1.2 Increasing initial- and boundary temperatures	15
3.1.3 Test case: The February 2016 Aalvik icing event (19.02.2016-26.02.2016)	16
3.1.4 The 2015-2016 winter season (01.11.2015-31.03.2016)	18
3.1.5 Ice accretion model	20
<b>4 Results and discussion</b>	<b>21</b>
4.1 Model verification	21
4.1.1 WRF	21
4.1.2 Ice accretion model	23
4.2 Synoptic analysis of the February 2016 Aalvik icing event	28
4.3 Geographical distribution of icing	30

4.4	The effects of increased initial- and boundary temperatures on key icing related variables . . . . .	32
4.4.1	Changes to humidity conditions and precipitation patterns . . . . .	35
	Precipitation . . . . .	36
	Cloud liquid water content . . . . .	37
4.5	Control vs. warm run icing . . . . .	38
4.5.1	Terrain height dependency . . . . .	41
4.5.2	Change in occurrence frequency of icing events . . . .	44
<b>5</b>	<b>Discussion and conclusions</b>	<b>47</b>
5.1	What made the difference? . . . . .	48
5.1.1	Temperature . . . . .	48
5.2	Future research . . . . .	51
	<b>Bibliography</b>	<b>53</b>

# Chapter 1

## Introduction

### 1.1 What is atmospheric icing?

Supercooled liquid water is commonly found in the atmosphere at temperatures between  $-15^{\circ}\text{C}$  and  $0^{\circ}\text{C}$ , both as cloud droplets and drizzle or rain. The supercooled water particles freeze immediately upon impact if they hit aircraft, power lines, wind turbines or any other object. This particular process is referred to as rime-icing. Ice accretion on structures may also occur due to collection of wet snow particles (wet snow accretion) and by deposition of water vapor (hoar frost). Each of these processes are generally referred to as *atmospheric icing*, a phenomenon that has been studied extensively during the past decades.

There are several examples in the literature portraying the potential harmfulness of atmospheric icing events. The most famous one is perhaps the freezing rain event in eastern Canada, 1998, also known as ‘the Great Ice Storm of 1998’. Massive damages to the power grid deprived more than two million people of electricity for weeks, as thousands of transmission towers collapsed due to heavy ice loads. The storm led to a total of 35 fatalities. On the other side of the Atlantic Ocean, inn Voss, Norway, 1961, rime ice coated power lines with record breaking ice loads of up to  $305\text{ kg/m}$  (Figure 1.1). Similar events, though less extreme, are observed every year in many countries at mid- and high latitudes.

The complex nature of icing events makes them hard to predict, as calculations of cloud physical processes in atmospheric models rely on simplifications and parameterizations. This leads to uncertainties regarding the total availability of atmospheric water, and subsequently the abundance of supercooled liquid water content (SLWC). However, the computational power of today’s super computers allows atmospheric models to apply increasingly more sophisticated microphysics schemes. In a recent study, Kringlebotn Nygaard, Kristjánsson, and Makkonen (2011) were able to predict SLWC with an absolute error of only  $0.08\text{g/m}^3$  using the Thompson microphysics scheme (Thompson et al., 2008) in the Weather Research and Forecasting (WRF) model. Supercooled LWC predictions of this caliber is crucial for skillful predictions of atmospheric icing events.





FIGURE 1.1: Rime ice on overhead power lines in Voss, Norway, 1961. This particular icing event led to the largest ice loads ever observed on power lines, with a maximum of 305 kg/m. [Photography by Olav Wist]

## 1.2 Atmospheric icing in a changing climate

As the climate is changing, and is expected to continue to do so, our understanding of atmospheric icing faces further challenges. How will the icing conditions be different in a future climate? Largely due to uncertainties regarding how a future climate may look like, this question is a difficult one to answer even with the most advanced tools available today. It is however a highly relevant question, as power lines and other exposed structures are built to withstand ice loads up to a certain threshold, and have a desired lifetime extending well into a period where the climate is expected to be different from what it is today.

Although the exact outcome of climate change is difficult to predict, some climate variables are very likely *not* to change due to physical constraints. Important to the atmospheric icing conditions is the fact that the distribution of relative humidity in the troposphere is believed to remain more or less constant (Intergovernmental Panel on Climate Change, 2014b; Allen and Ingram, 2002). Consequently, increased global temperatures would imply an exponential increase in specific humidity according to the Clausius-Clapeyron relation (see chapter 2.3). Increased values of water vapor content are already evident from observations (Trenberth, 2011),

and numerical studies have shown that this may lead to higher precipitation rates in regions where precipitation rates are already high, including the mid- and high latitudes.

The aim of this study is to investigate the possible effect(s) that increased global temperatures may have on atmospheric icing conditions in the complex orography of western Norway, given the constraints discussed above. With westerly winds frequently coming in from the Atlantic Ocean, this particular region is highly exposed to rime-icing, and has consequently suffered collapses of several power lines and even transmission towers throughout the past decades. In this simplified representation of a future climate - could higher specific humidities lead to greater concentrations of (supercooled) LWC and possibly enhanced icing events, or will the effect of higher temperatures suppress ice growth sufficiently to give less icing than in the present climate?

The present study is a part of the WISLINE project (Wind, Ice and Snow Load Impacts on Infrastructure and the Natural Environment), an ongoing research program conducted by The Norwegian Meteorological Institute in collaboration with other partners, including the Department of Geosciences at the University of Oslo and Kjeller Vindteknikk. One objective of WISLINE is to downscale data from climate models using the AROME model, where descriptions of microphysical processes similar to those of the Thompson scheme will be applied in order to quantify climate change impact on technical infrastructure caused by icing. By utilizing output from climate models, additional aspects of climate change, such as changes to large scale circulation patterns, are also taken into account. This approach could therefore give a more complete overview of future icing conditions, whereas the simplified approach of this study aims to investigate impacts of certain climate change aspects only, namely increased temperature and specific humidity.

### 1.3 Thesis overview

In the present study, WRF was used with a similar setup to that which was applied in Kringlebotn Nygaard, Kristjánsson, and Makkonen (2011) to simulate the 2015-16 winter season with increased initial- and boundary temperatures. The model output data was then used to perform extensive icing computations that was compared to those obtained from a control simulation. Shorter test simulations were also made, where the calculated ice loads were compared to observations for model verification. The following chapter will present necessary background theory on atmospheric ice accretion on structures, and how structural ice growth rates are modelled numerically. In Chapter 3 the setup of the WRF model will be presented in further detail, as well as the specifics of the ice accretion model that was used. In Chapter 4, results from all model runs will be presented and discussed, illustrating differences both within meteorological variables as well as icing calculations between the simulations. Conclusions are drawn in Chapter 5, where suggestions to further research will also be presented.

## Chapter 2

# Theory

In this chapter we will briefly go through the meteorological aspects of icing events, and further how ice accretion can be modelled numerically. The latter is a rather complex process, and requires attention to a whole array of different physical properties and processes. Regardless, a good representation of the local meteorological variables including temperature, wind speed, droplet sizes and number concentrations is key to successful icing predictions, and is still the most significant source of uncertainty (particularly the latter two).

### 2.1 How do icing events occur?

Depending on the weather situation, icing may either occur in-cloud or during precipitation. Geographically, the phenomenon is most pronounced at mid- and high latitudes, but has also been observed in high altitude regions of e.g. Spain, South Africa and Latin America (Fikke, Kristjánsson, and Kringlebotn Nygaard, 2008).

#### 2.1.1 In-cloud icing

In-cloud icing is a phenomenon that may only occur when the icing object is in direct contact with a cloud containing supercooled liquid water drop(let)s. Supercooled water can be found in any cloud at temperatures between  $-38^{\circ}\text{C}$  and  $0^{\circ}\text{C}$  (mixed phase clouds), as homogeneous nucleation of ice only occurs at  $T \simeq -38^{\circ}\text{C}$  or lower (Lamb and Verlinde, 2011). Ice initiation in mixed phase clouds requires the presens of ice nuclei (IN), a particular sub-group of aerosols that, due to their ice-like structure, may trigger supercooled droplets to freeze at temperatures of  $T > -38^{\circ}\text{C}$ . This may happen in cases were a) the IN collides with the droplet (contact nucleation), or b) the IN is immersed within the droplet (freezing nucleation), both of which are termed hetrogeneous ice nucleation. The ratio of supercooled droplets that freeze to those that remain liquid in a mixed-phase cloud depends on the available amount of IN and the degree of supercooling. Only the most effective IN enable ice nucleation at temperatures close

to  $0^{\circ}\text{C}$ , and the availability of IN in general is rather limited. Supercooled liquid water is thus commonly found in clouds at temperatures between  $-15^{\circ}\text{C}$  and  $0^{\circ}\text{C}$ .

Human installations such as power lines and wind turbines can be exposed to in-cloud icing in one of two ways; either the structure in question is tall enough to penetrate the base of the cloud, or the cloudbase is below groundlevel in which case the structure is surrounded in what is then a fog of supercooled water particles. In-cloud icing is most commonly observed in cold, mountainous regions, where orographic lifting processes frequently produce clouds that are in close contact with the higher grounds. In extreme cases, persistent weather situations may cause in-cloud icing events to last for weeks (Kringelebotn Nygaard, Kristjánsson, and Makkonen, 2011), allowing for continuous growth and the development of devastating ice loads.

### 2.1.2 Freezing rain/drizzle and wet snow accretion

During freezing rain/drizzle or wet snow accretion events, ice can also form on structures that are not in direct contact with clouds. Freezing rain is a term that is used when supercooled rain- or drizzle drops freeze upon impact with the ground or any type of object in their path. This may cause serious hazards to traffic as well as problems involved with ice accretion on structures. The meteorological conditions that are necessary for the production of freezing rain/drizzle are described in Zerr (1997). In the presence of a temperature inversion, a snow particle may melt before it cools back to a temperature below freezing point on its way towards the ground. In order for this to happen, the vertical temperature profile must resemble the one depicted in 2.1. Depending on whether or not the ice particle melts completely in what is referred to as the *melting layer*, it may either refreeze or become supercooled, but remain liquid, in the *refreezing layer* below. The latter is then what we call freezing rain. If the ice particle only partially melts in the melting layer, the remaining ice may act as ice nuclei and cause the particle to refreeze before it reaches the ground. Should the ice melt completely, however, a more substantial supercooling would be necessary in order for the particle to refreeze, making it more likely to reach the ground as a supercooled liquid water particle. The ice that is formed on structures during freezing rain/drizzle events is usually glaze ice.

Ice may also form on structures by collection of wet snow particles, a phenomenon usually referred to as wet snow accretion. Whereas a completely frozen snow particle (a 'dry' snow particle) will effectively bounce off of the icing object upon impact (Makkonen, 1989), the liquid layer on the surface of a wet snow particle will cause it to stick more easily. Wet snow

accretion may occur in unstable air masses when snow particles fall from a cold layer above, into a warmer layer close to the ground.

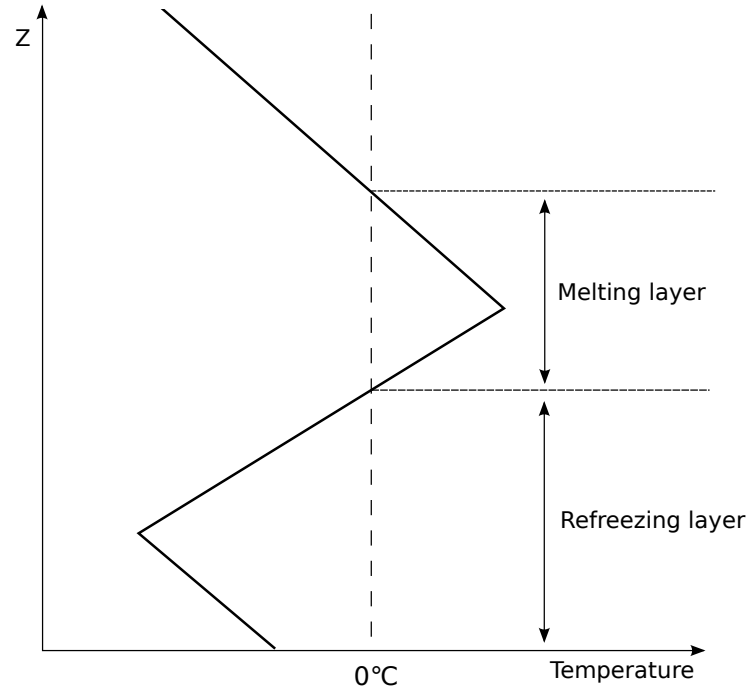


FIGURE 2.1: Conceptual temperature profile during a freezing rain/drizzle event.

### 2.1.3 Dry growth vs. wet growth

Depending on the temperature of the environment and the surface heat balance of the icing object (see section 2.2.1), different types of ice may form. When the surface is completely frozen, impinging water particles will freeze almost immediately, and we have what is called dry growth conditions. The ice that is formed during dry growth is called *rime*, and is often white and opaque (Figure 1.1). Should the surface of the icing object be coated in a layer of liquid water, however, ice would grow under so-called wet growth conditions. This type of growth will produce *glaze*, a more dense and transparent type of ice.

## 2.2 Models of ice growth on structures

Ranging in complexity from simple, analytical models that can be solved with pen and paper, to numerical models that require the computational power of super computers, several models for the growth of atmospheric ice on structures has been developed throughout the last 60 years or so. An

overview of the progression in this particular field is reviewed in Lozowski and Makkonen (2005). The necessary simplifications and empirical representations of physical processes needed to be able to calculate ice loads by hand, makes analytical models unsuitable for practical purposes. However, as stated in Lozowski and Makkonen (2005), since errors in icing rates tend to average out over time, analytical models have some validity in predicting accumulated ice accretion, and have been widely used for this reason despite their deficiencies. An example of such a model is  $R = cV$  (Lozowski and Makkonen, 2005), which gives the rate of rime-icing  $R$ , where  $V$  is wind speed. With wind speed being the only dependent variable, remaining deciding factors like LWC and the efficiency with which the particles collide with the icing object are left to be accounted for by the constant,  $c$ .

### 2.2.1 Growth rate of ice on a standard icing object

The airflow around structures of intricate shapes can become arbitrarily complex, which means that the calculations of ice growth upon them can too. It is therefore common to compute atmospheric ice accretion on so-called standard icing objects, which is defined as a 1 meter long cylinder with a diameter of 30 mm (the typical diameter of an overhead power line). The following section will review the theory of ice growth on a standard icing object as it is described in Makkonen (2000).

Ice can not only form on structures by impinging water particles that freeze (in the case of liquid particles) or sticks to the surface of the object (in the case of wet snow particles) upon impact, but also directly by deposition of water vapor (hoar frost). However, the latter can usually be neglected when the aim is to calculate significant ice loads, as the rate of ice growth due to deposition of water vapor is much smaller than that of impinging water droplets and snow particles. Therefore, the growth rate of ice is a result of the flux density of water particles, and is given by

$$\frac{dM}{dt} = w\mathbf{v}A \quad (2.1)$$

where  $M$  is the mass of ice on the structure,  $w$  is the mass concentration of particles and  $\mathbf{v}$  is the velocity of the particles relative to the cross-sectional area of the structure,  $A$ . However, this equation would only be exact if the following cases were true: Firstly, every particle whose original velocity vector is pointing towards the object would actually have to *hit* the object, and not follow the airstream around it. Secondly, every particle that *does* hit the object would have to stick to it and not bounce off after impact. Lastly, all of these particles would then have to freeze readily in order to not fall off of the object due to wind stress or gravity. Considering the nature of the atmosphere, this is rarely (if ever) the case. Therefore, *collision efficiency*,

*sticking efficiency* and *accretion efficiency*, hereafter denoted as  $\alpha_1$ ,  $\alpha_2$  and  $\alpha_3$ , respectively, will have to be included in equation 2.1.

### **Collision efficiency, $\alpha_1$**

The relative magnitude of the aerodynamical drag and inertia forces experienced by the particles as they approach an object determines whether the particle will collide with the object or not. Since air cannot flow through a solid object, it has no other choice but to go around. Smaller water particles with little inertia tend to follow the air stream closely, and often avoid any contact with the object. On the other hand, a heavier particle with a stronger inertial force will to a larger degree follow its original path towards the object, and have an increased chance of collision. Consequently, if one is to calculate the exact collision efficiency for a population containing particles of all sizes and shapes, one would have to calculate the individual trajectory for all particle sizes represented in the population. This is practically impossible for a number of reasons, with number one being that the exact size distribution of a particle population is rarely known.

Even when reducing the number of trajectory calculations substantially by dividing particles into size bins, the process is cumbersome and computationally expensive. However, previous studies have shown that good results can be obtained by utilizing different monodisperse particle size distributions, with the use of the median volume diameter (MVD) being the most prominent one. Finstad, Lozowski, and Makkonen (1988) showed that collision efficiency for a cylinder can be calculated with an absolute error as small as 0.02 compared to a more advanced spectrum weighting approach by using the MVD approximation. Furthermore, Makkonen (2000) states that, in most practical applications, collision efficiency can be assumed to be unity for the larger members of the particle population (such as rain drops and wet snowflakes) due to the strong dependence on particle size.

### **Sticking efficiency, $\alpha_2$**

Whether or not a colliding particle will stick to the icing object after impact depends strongly on the type of particle. Whether the surface of the icing object is completely frozen (dry growth) or it is covered by a liquid water layer (wet growth), a supercooled liquid water droplet will not rebound after collision. Instead, it will either freeze almost immediately given the first case, while in the latter case, the droplet will spread out and merge with the liquid layer. Hence, the sticking efficiency for liquid water droplets can be assumed to be unity. However, as they so often do, snow particles tend to complicate the situation. The details of sticking efficiency for snow particles is not yet well understood, and remains as an uncertainty in ice accretion



modelling. Depending on impact velocity, humidity and temperature conditions as well as how wet the particle is, the sticking efficiency of snow particles can range from almost zero to unity. Dry particles tend to bounce very efficiently, while if there is a liquid layer on the surface of the snow particle, it will stick more easily. The sticking efficiency will also increase with lower impact speeds, and simple approximations such as  $\alpha_2 = 1/v$  where  $v$  is the wind speed and  $\alpha_2 = 1$  if  $v < 1\text{m/s}$  have been suggested.

### Accretion efficiency, $\alpha_3$

The accretion efficiency is the ratio of particles that freeze and contribute to an objects ice load to the particles that stick to the object, but do not freeze. As mentioned above, supercooled droplets will always freeze readily under dry growth conditions, yielding an accretion efficiency close to one. Under wet growth conditions, the accretion efficiency depends on the freezing rate of the liquid layer on the surface of the icing object. The amount of water that is allowed to freeze is decided by the heat balance of the icing surface, and in particular, the rate at which the latent heat of freezing can be transported away from the surface to the surrounding air. The surface heat balance in the case of wet-growth can be written as

$$Q_f + Q_v = Q_c + Q_e + Q_l + Q_s \quad (2.2)$$

where

$Q_f$  = latent heat of freezing

$Q_v$  = frictional heating of air

$Q_c$  = loss of sensible heat to air

$Q_e$  = heat loss due to evaporation

$Q_l$  = heat loss due to the warming of the supercooled water to the freezing point

$Q_s$  = heat loss due to radiation

When the heat loss terms in equation 2.2 are larger than the heating terms,  $\alpha_3$  becomes positive and the water at the boundary between the ice and the liquid layer is allowed to freeze.

### Icing rate

When collision, sticking and accretion efficiencies are accounted for, the growth rate of ice on a standard object is given by

$$\frac{dM}{dt} = \alpha_1 \alpha_2 \alpha_3 w \mathbf{v} A. \quad (2.3)$$

Equation 2.3 has a somewhat peculiar dependency on the size of the icing object. As the surface area,  $A$ , is really a function of the ice mass,  $M$ , the ice growth rate (in the case of  $\frac{dM}{dt} > 0$ ) will seemingly increase with time as  $A$  gets bigger (assuming  $w, v = \text{constant}$ ), yielding a positive feedback. However, the collision efficiency has an opposing effect; as the diameter of the cylinder gets larger, the airflow tends to deflect incoming water particles away from the object more easily, causing  $\alpha_1$  to decrease (unless the size of the water particles are sufficiently large, in which case  $\alpha_1 = 1$  and the effect of  $A$  will dominate).

## 2.3 Increased temperature and the impact on humidity conditions

In the introduction it was stated that an increase in temperature would imply an exponential increase in specific humidity, given that the relative humidity remains constant. As this forms the basis for the present study, it is appropriate to take a closer look at why this is the case. The physics behind this theory is described by the Clausius-Clapeyron equation for liquid water, yielding the relationship between temperature and the water vapor pressure:

$$\frac{de_s}{dT} = \frac{l_v e_s}{RT^2}, \quad (2.4)$$

where  $e_s$  is the saturation water vapor pressure,  $l_v$  is the latent heat of vaporization,  $R$  is the gas constant for water vapor and  $T$  is the temperature. By keeping  $l_v$  constant<sup>1</sup>, equation 2.4 can easily be integrated to give

$$e_s(T) = e_0 \exp\left(\frac{l_v}{R} \left(\frac{1}{T_0} - \frac{1}{T}\right)\right), \quad (2.5)$$

where  $e_0 = 611 \text{ Pa}$  is the water vapor pressure with respect to a mixture of pure water and ice at  $T = T_0 = 273.15 \text{ K}$ . In Figure 2.2,  $e_s(T)$  is plotted as expressed in equation 2.5. Since  $e_s(T)$  is the water vapor pressure at which a parcel of air becomes saturated at a given temperature, the relative humidity is constant ( $RH = \frac{e(T)}{e_s(T)} 100\% = 100\%$ ) along the blue curve in Figure 2.2. Hence, if the relative humidity is to be unchanged, an increase of temperature would imply that the water vapor pressure of the air parcel would have to increase accordingly. This is made possible only if the ratio of the mass of water vapor to the total mass of the air parcel (specific humidity) is increased as well. Notice also that if the temperature is increased from  $T$  to  $T + \Delta T$ , the slope of  $e_s(T)$  implies that the increase in water vapor pressure, and thus specific humidity, will become greater with higher initial

<sup>1</sup>The latent heat of vaporization is in reality a function of temperature, however, keeping it constant is a good approximation for atmospheric applications (Lamb and Verlinde, 2011).

air parcel temperatures. Consequently, increased temperatures at constant relative humidity leads to an exponential increase in specific humidity.

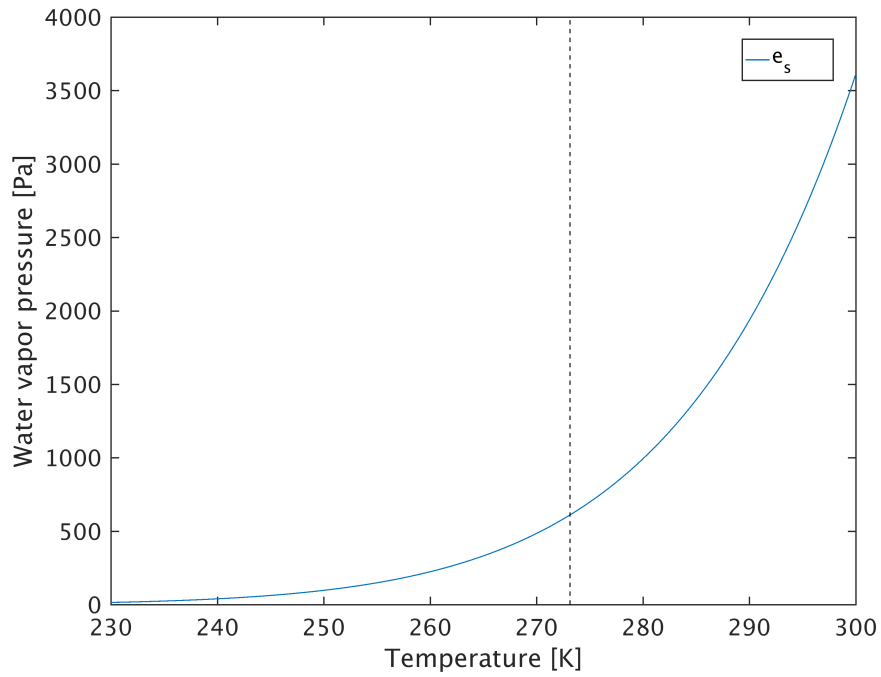


FIGURE 2.2: The saturation water vapor pressure,  $e_s$ , as a function of temperature (the Clausius-Clapeyron relation).

## Chapter 3

# Methods

The variables that are included in equation 2.3, and are thus necessary for icing computations, are not all available from observations. Furthermore, the few variables that are indeed observed regularly are only available at certain locations, and the quality of the observations can be poor during icing events due to ice accretion on instruments. Hence, the use of a numerical weather prediction (NWP) model is therefore required to provide input data to the ice accretion model (IAM). This chapter will give an overview of the WRF model setup, as well as some specifics regarding the IAM that was used.

### 3.1 Model setup

All simulations in this study are made using version 3.8.1 of the Weather Research and Forecasting (WRF) model. WRF is a state of the art numerical weather prediction model designed for a wide range of mesoscale applications. It is widely used for both research and forecasting purposes across the world, and was developed by the National Center for Atmospheric Research (NCAR) in collaboration with other organisations.

The model simulations are forced with ERA-Interim data obtained from the European Centre for Medium-Range Weather Forecasts (ECMWF). ERA-Interim is an atmospheric reanalysis covering the entire globe from 1979 until present, and is available four times a day with a spatial resolution of approximately 80 km. The WRF Preprocessing System (WPS) use the reanalysis to create an initial field for all model domains (optional for nested domains<sup>1</sup>), and further to provide boundary conditions for the outermost (parent) domain every sixth hour for the duration of the simulation.

In mesoscale weather prediction models such as WRF, sub-grid processes like e.g. cloud microphysics and boundary layer physics have to be parameterized using different numerical schemes. As all the available

---

<sup>1</sup>Nesting is a technique that enables finer-resolution model runs in a smaller region. One or more high resolution ‘child’ domains may be nested within a coarser-resolution ‘parent’ domain. The parent domain will then provide boundary conditions to the respective child domain

schemes have their advantages and disadvantages, they must be chosen carefully based on the type of weather situation that is being simulated and the availability of computational power. The different parameterization schemes that were used in the present study are listed in Table 3.1. No cumulus parameterization scheme was applied<sup>2</sup>.

Cloud microphysics	Thompson scheme
Planetary boundary physics	Mellor-Yamada-Janjic Scheme
Shortwave radiation	Dudhia Shortwave Scheme
Longwave radiation	RRTM Longwave Scheme
Land surface physics	5-layer Thermal Diffusion Scheme
Surface layer physics	Eta Similarity Scheme

TABLE 3.1: List of parameterization schemes used in the WRF simulations.

### 3.1.1 Cloud microphysics scheme

As was mentioned earlier, the validity of structural icing computations rely heavily on the quality of the input data, and in particular on the available amount of supercooled liquid water content (SLWC). Consequently, the choice of parameterization scheme concerning cloud microphysics was made with extra care. Common for many microphysics schemes is the tendency to predict too much ice phase rather than liquid at sub-zero temperatures, thereby substantially underestimating the occurrence frequency of SLWC in the atmosphere, hence underestimating icing. In order to investigate the ability to predict in-cloud icing at ground level using WRF, several simulations were made by Kringlebotn Nygaard, Kristjánsson, and Makkonen (2011) applying three different microphysics schemes. The Thompson scheme (Thompson et al., 2008) systematically gave the most skillful predictions of SLWC when compared with measurements, and was therefore also used for this study. In particular, the best results were obtained when the Thompson scheme was applied in combination with high, horizontal model resolution. The latter was stated to be especially true when running simulations in mountainous regions where orographic effects are an important factor for the abundance of LWC.

Available microphysics schemes differ in complexity by how many moments of the droplet size distribution that are being explicitly *predicted* by the model, as opposed to being prescribed by statistical distributions. A

<sup>2</sup>A cumulus parametrization scheme should generally be applied to domains with a spatial resolution of about 5km or lower. For icing simulations however, tests performed at Kjeller Vindteknikk have shown that the use of a cumulus parametrization scheme in the outermost domain only leads to unnecessary complications, and has no significant impact on results in the finer scale nested domain(s).

one-moment scheme is thus limited to predicting one microphysical moment (usually mass), while double-moment schemes will predict two microphysical moments (usually mass and number concentration) and so on. The Thompson scheme is in this regard essentially a one-moment scheme, with the exception of the variables cloud ice and rain, where the number concentration is predicted in addition to the mass (mixing ratio). The remaining (one-moment) hydrometeor variables for which only mixing ratio is predicted are cloud water, snow and graupel. The scheme was designed to better resemble double- or higher order schemes while keeping computational costs on the level of one-moment schemes by using lookup tables for the microphysical moments that are not explicitly predicted.

### 3.1.2 Increasing initial- and boundary temperatures

The gist of the experiments made in this study is to compare icing calculations based on the output from two different WRF simulations, one of which is forced with increased initial- and boundary temperatures and the subsequent rise in specific humidity (see Chapter 2.3). Each case, i.e. the 2015-16 winter season and the shorter test simulations of the February 2016 Aalvik icing event (see next section), will thus consist of one control and one perturbed run. The latter will hereafter be referred to as the 'warm run/simulation'.

A constant,  $\Delta T = 2^\circ\text{C}$ , was added to all temperature-relevant variables (the 3D temperature field, 2m temperature, 2m dew point temperature, sea surface temperature, skin temperature as well as the temperature of all four soil levels), of the warm run input datasets, but the relative humidity was kept constant. The choice of  $\Delta T$  was based upon the long-term climate projections from IPCC's Fifth Assessment Report (Intergovernmental Panel on Climate Change, 2014a). Global annual mean surface air temperature increase projections based on four different emission scenarios from this report are shown in Figure 3.1. Considering that e.g. power lines are built to last for 70+ years, the year 2100 was chosen as a point of reference. The choice of  $\Delta T = 2^\circ\text{C}$  is not as 'pesimistic' as it may seem from a quick glance at Figure 3.1, as it is also evident from climate models that the magnitude of the temperature increases will be amplified towards the poles, and even more so during winter.

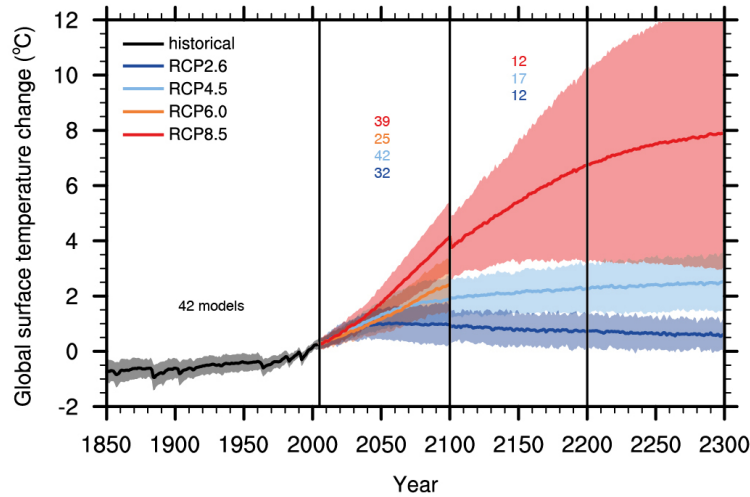


FIGURE 3.1: Projected increase of global annual mean surface air temperatures based on four different Representative Concentration Pathways (RCPs). Figure taken from AR5 (Intergovernmental Panel on Climate Change, 2014b).

After the input data had been horizontally interpolated to fit the model domain in the WRF Preprocessing System (WPS), the heights of the vertical levels in the warm simulations were adjusted due to thermal expansion and specific humidity was increased in accordance with equation 2.4.

### 3.1.3 Test case: The February 2016 Aalvik icing event (19.02.2016-26.02.2016)

Before embarking on the full 2015-16 winter season, shorter test simulations (control and warm) were made in order to verify that the ice accretion model was able to produce reasonable results based on the WRF setup that was used. During a four day time period in February 2016, considerable ice accretion was recorded by an observational instrument at Aalvik (1085 m.a.s.l.) in Hordaland, Norway. The instrument (3.2), provided by Kjeller Vindteknikk, is designed to measure ice loads on a standard icing object, which makes the observations highly suitable for model verification.

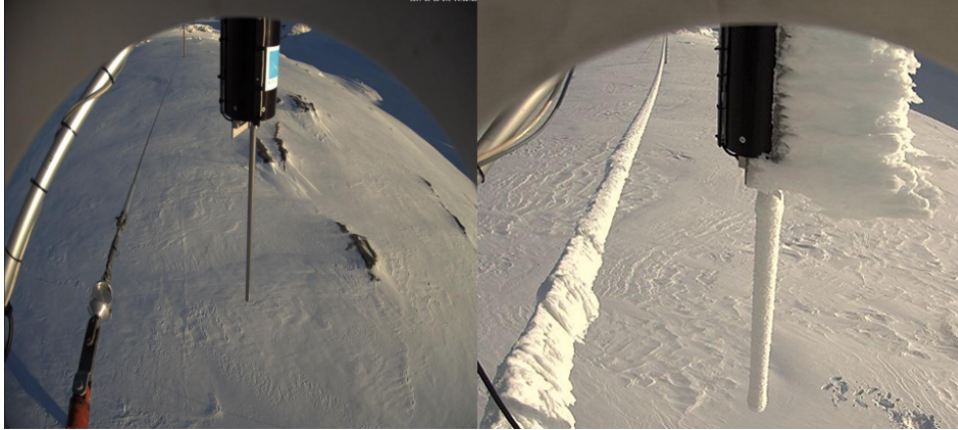


FIGURE 3.2: Pictures showing the instrument at Aalvik measuring ice growth on a standard icing object. The vertical cylinder is slowly rotating, allowing ice to grow more or less uniformly on its surface independent of wind direction. Photos provided by Kjeller Vindteknikk.

In order to properly resolve the mountainous terrain of western Norway, and hence orographic lifting processes, the simulations were made with relatively high spatial resolution. This was obtained by setting up the model with a total of three domains (Figure 3.3) using the nesting technique described earlier. The largest and outermost (parent) domain covers the southern part of Scandinavia as well as the North Sea and parts of Great Britain. This serves as a parent for a second domain covering the southwest part of Norway, which in turn serves as a parent for the innermost domain covering a  $133 \text{ km} \times 137 \text{ km}$  area surrounding Aalvik where we have available observations of icing. The spatial resolution of the domains was set to 16 km, 4 km and 1 km, respectively. Exchange of information at the boundaries between domains were done using a one-way nesting technique, meaning that the child domains receive input from their respective parents, but no information is being fed back to the parent (two-way nesting).



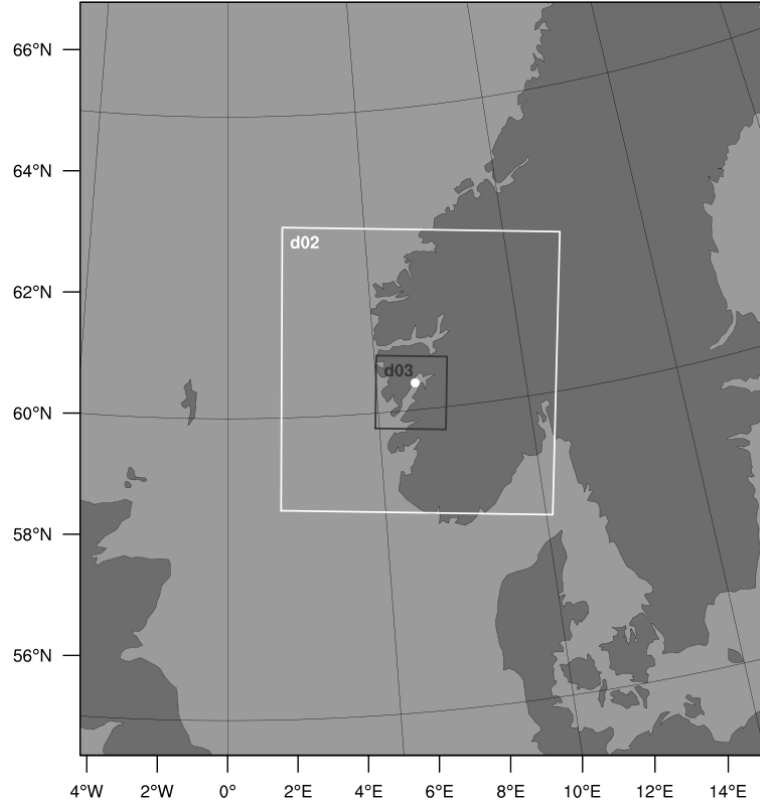


FIGURE 3.3: Map showing locations of all three domains used in the WRF simulations. The white dot in the innermost domain shows the location of the Aalvik station.

The test simulations were run for a 7 day period covering the aforementioned icing event, starting at 00:00:00 UTC on February the 19th, 2016. Strong, vertical winds due to steep hillsides caused violations of the Courant-Friedrichs-Lewy (CFL) condition when using time steps of two seconds or larger for the innermost domain, forcing us to go all the way down to one second to avoid numerical stability issues. Another tweak that helped to avoid the stability problems was to turn on the w-damping option that applies a Rayleigh damping term to the vertical velocity equation when the model detects that the CFL condition is about to be violated.

#### 3.1.4 The 2015-2016 winter season (01.11.2015-31.03.2016)

The model setup for the winter season simulation was kept more or less the same as for the test case, however, an additional tweak in the preprocessing system was necessary in order to keep the computation time down. Due to the small time step in the 7 day test simulations, the computation time using the Abel computer cluster located at UiO was about two days. This would imply a running time of more than 40 days for a five month winter season, which was not feasible considering our time frame. As mentioned

before, the biggest issues occurred with excessively strong updrafts caused by steep hillsides. There is an available option in WPS that smooths out the model terrain, and can be applied to the problematic domain(s) to allow for larger time steps. However, smoothing out the entire domain would make the high spatial resolution lose some of its purpose. Instead, we were able to apply a scheme provided by Kjeller Vindteknikk that smooths out only a small area surrounding the most problematic grid points, leaving the lion's share of the domain 'untouched'.

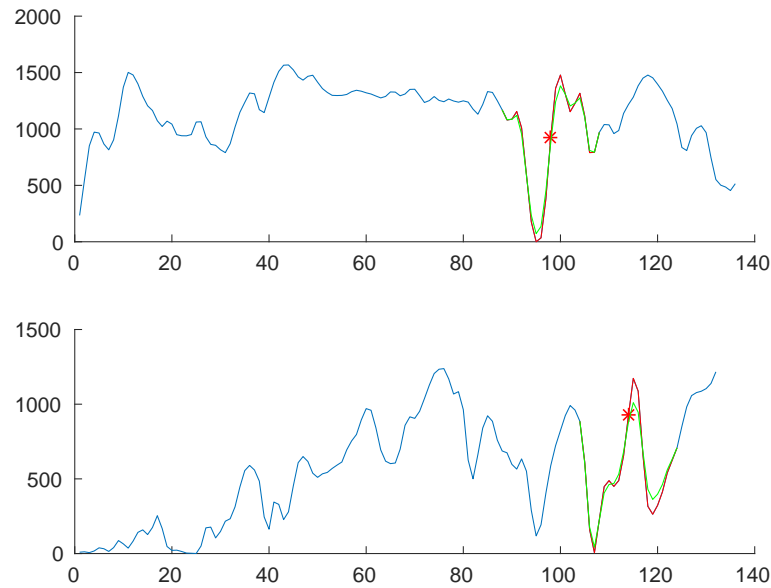


FIGURE 3.4: Upper panel: South-north cross section through one of the smoothed areas. Lower panel: West-east cross section through the same smoothed area as in upper panel. On the x-axes are the grid points of the innermost domain, and the y-axes are showing terrain height in meters. The red stars point out the grid point around which the terrain has been smoothed, and the green curves show the terrain height after smoothing.

After applying this scheme to a total of four grid points, the model ran successfully without any stability issues using time steps of 4 seconds for the innermost domain (still with a 1km spatial resolution), reducing the computation time substantially. This, in addition to increasing the number of CPUs to 32 (as opposed to 16 for the test case) resulted in a running time of approximately six days for the full winter season simulations. Cross sections of the changes in terrain height through one of the problematic grid points are shown in Figure 3.4, and a map of the entire innermost domain showing the height difference of the terrain before and after the smoothing is shown in Figure 3.5. As the region is dominated by westerly airflow, the smoothed area in Figure 3.5 is downstream of all key locations, e.g.

Aalvik, Folgefonna as well as both weather stations used for model verification (see Chapter 4.1). Therefore, the terrain modification did not have any major impact on the results.

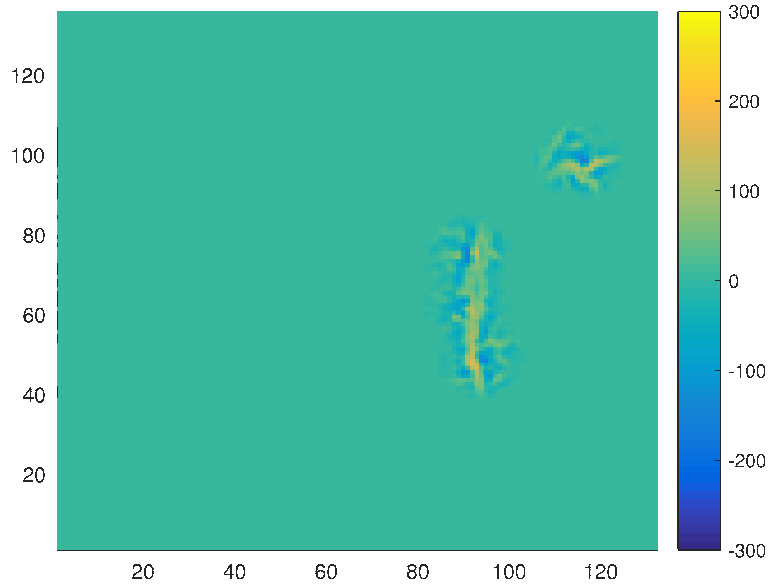


FIGURE 3.5: Difference between model terrain height (m) in the innermost domain before and after smoothing process.

### 3.1.5 Ice accretion model

The ice accretion model (IAM) that was used utilizes the theory described in chapter 2.2, and was provided by Kjeller Vindteknikk. Icing calculations were made based on equation 2.3, yielding the rate of ice growth on a standard icing object. The collision efficiency is calculated using the MVD approximation, and the sticking efficiency is set to unity. Sinks include both melting, which occurs when the temperature of the environment is above  $0^{\circ}\text{C}$ , and sublimation. Since ice shedding is not included in the model, sublimation is the only ice removing mechanism at temperatures below freezing.

The IAM also includes a vertical interpolation routine which can be useful when comparing calculated ice loads to observations. As model grid-points rarely match the exact location of the observation site, there can be a substantial height mismatch between the true site and the closest grid-point, especially in mountainous areas. In theory this means that in some situations, the observation site is located above cloudbase while the closest gridpoint is not (or vice versa), leading to a misrepresentation of the icing conditions in the model. This is solved by doing an interpolation of all variables needed for icing calculations between the two vertical levels of the model that are closest to the true height of the observation site.

## Chapter 4

# Results and discussion

In this chapter, results from all model simulations will be presented and discussed. The first section will review model performances, and results from both WRF and the ice accretion model are verified against observations. In the proceeding sections, output from the WRF winter season simulations is used to provide insight into how key icing-related variables responded to the temperature increase. The chapter concludes by providing extensive control vs. warm run comparisons of simulated ice accretion.

### 4.1 Model verification

#### 4.1.1 WRF

Temperature and wind speed from the WRF control simulation were verified against hourly observations from two different weather stations in order to ensure that the model produced reasonable results. The weather stations are located at Flesland (48 m.a.s.l.) and Kvamskogen (455 m.a.s.l.) respectively, and are operated by the Norwegian Meteorological Institute. Figure 4.1 shows modelled vs. observed wind speeds at the Flesland station for all five months. The two curves match seemingly well, although the model is slightly positively biased, mainly in periods with little wind. The locations of both weather stations as well as the Aalvik observation site are shown in Figure 4.2.

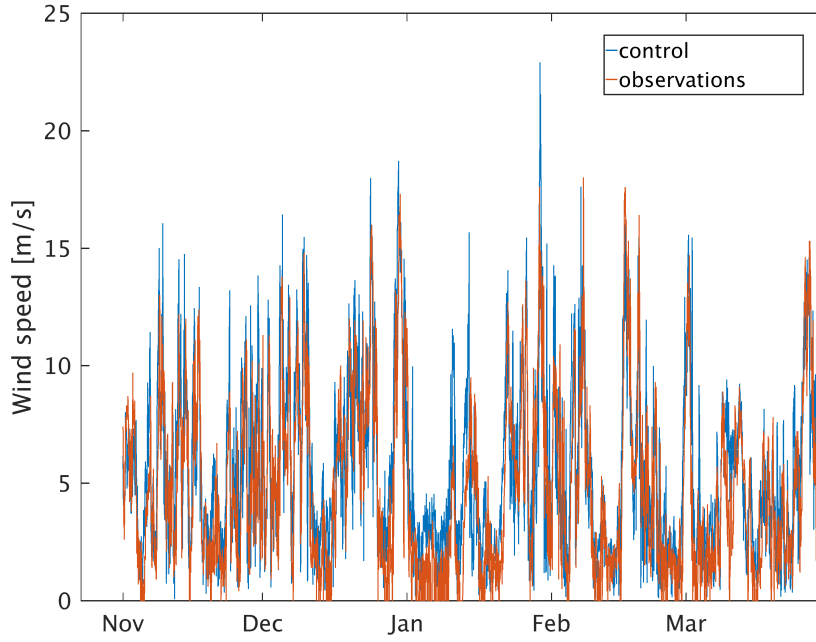


FIGURE 4.1: Control run wind speeds vs. observations from Flesland weather station (48 m.a.s.l.).

Temperature and wind speed correlations, as well as model biases, can be seen in table 4.1. Although the model shows a strong correlation with the observations, it has a warm bias. This is due to misrepresentations of the coldest periods, which is consistent with the findings of García-Díez et al. (2013), where seasonal dependencies of WRF biases and their sensitivity to PBL schemes were studied. Out of the three PBL schemes that were tested, the Mellor-Yamada-Janjic scheme (which was used in this study) was among the two schemes that had the smallest warm bias over Europe during winter. It therefore seems unlikely that a different choice of PBL scheme would have reduced the warm bias in our simulation. The station at Kvamskogen lacked a total of 37 wind speed measurements (1.02% of the total possible measurements), and these were excluded from the calculations.

Station	T corr	FF corr	T bias	FF bias	model hgt	station hgt
FLESLAND	0.87	0.77	1.81 °C	0.67 m/s	37m	48m
KVAMSKOGEN	0.82	0.59	2.08 °C	1.64 m/s	508m	455m

TABLE 4.1: Model biases and correlations of temperature (T) and wind speed (FF) between the control run and observations.



FIGURE 4.2: Map of approximately the same area that is covered by the innermost model domain. Leftmost triangle: Flesland weather station (48 m.a.s.l.). Rightmost triangle: Kvamskogen weather station (455 m.a.s.l.). Red circle: Aalvik observation site (1085 m.a.s.l.). The map is obtained from [www.norgeskart.no](http://www.norgeskart.no).

#### 4.1.2 Ice accretion model

Just like with the temperature and wind speed computations from WRF, calculated ice loads from the ice accretion model were compared to observations in order to verify that the model was capable of producing reasonable results. This section provides figures comparing ice load calculations with measurements recorded during the February 2016 Aalvik icing event. For clarity, the 7 day test simulation and the full winter season simulation will hereafter be referred to as the 'short run' and the 'long run', respectively. Needless to say, all comparisons were made with icing calculations based on the output from the control simulations.

Figure 4.3 shows a comparison between calculated ice loads from the short run, with and without height correction (see chapter 3.1.5), and the observed ice accumulation. Here, the height of the model terrain in the grid point closest to the observation site is 985m while the true height of the observation site is 1085m, a difference of 100m. This is due to an inevitable mismatch between the location of the observation site and the closest model grid point, as well as the limited representation of the real world topography in the model. Although the height corrected curve has somewhat of a head start, it follows the observation curve quite closely. The uncorrected curve captures the early melting episode just prior to the icing event very

well, but the rate of the proceeding ice growth is far less than that of the observations. The initial ice load was prescribed to 900g/m in the ice accretion model to fit the observations. The sudden 'jump' in the observation curve that can be seen between the 02/23 and the 02/24 mark is due to ice shedding, i.e. ice breaking off of the instrument.

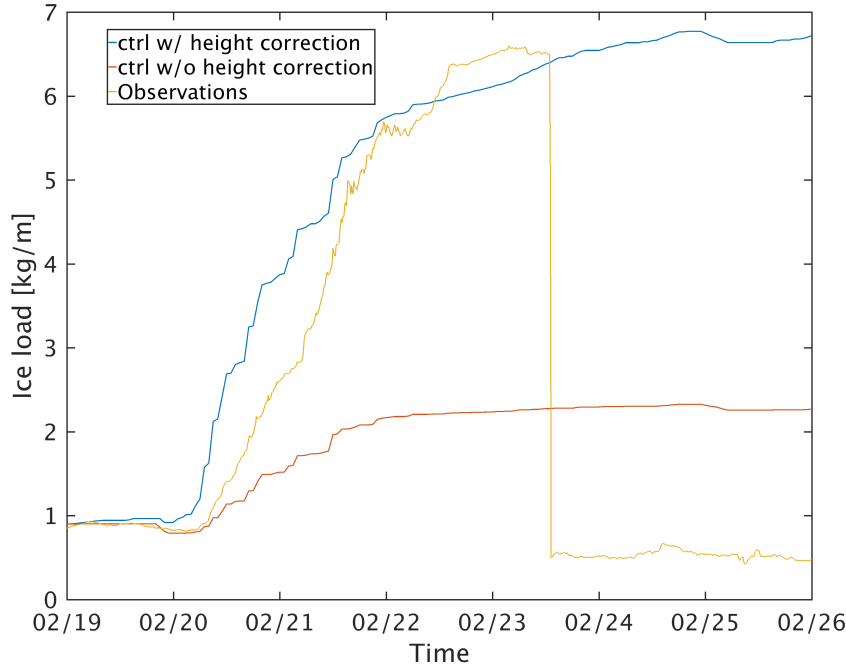


FIGURE 4.3: Ice accumulation during the February 2016 Aalvik icing event. Blue and red curves show short run calculations with and without height correction, respectively. The yellow curve shows observed ice accumulation, and the sudden jump between the 02/23 and the 02/24 mark is due to ice shedding (ice breaking off of the instrument).

It is evident from Figure 4.3 that the added lifting of the height correction routine was necessary in order for the IAM to properly recreate the observed icing event. However, while this routine was easy to perform for the seven day test case simulation, we were not able to apply it to the entire winter season. Due to the sheer amount of output data, only values from the lowest model level were stored from the five month winter season simulations, hindering the possibility of a vertical interpolation between two vertical levels. Consequently, icing computations based on the long run can be expected to yield underestimated ice loads in areas where the model terrain is substantially lower than the true terrain, and vice versa. The number of icing episodes in either simulation could potentially also be different from what it would have been with height correction due to situations where e.g. the lifting condensation level is somewhere in-between

the model height and the height of the real terrain. Nevertheless, the primary aim of this study was to investigate the icing *differences* between the warm run and control. However, any icing differences between the uncorrected simulations would only be representative of the real world if the absolute differences, particularly in cloud LWC, between the two simulations were the same at both heights. During the added lifting/lowering of the height correction routine, the saturation water vapor pressure will decrease/increase more rapidly in the warm run compared to the control due to the exponential nature of the Clausius-Clapeyron relation (see Chapter 2.3). However, if the height difference between the model and the real terrain is not too great, the relationship between temperature and saturation water vapor pressure can be assumed to be linear. In this case the absolute difference in cloud LWC between the two simulations would be the same at both heights.

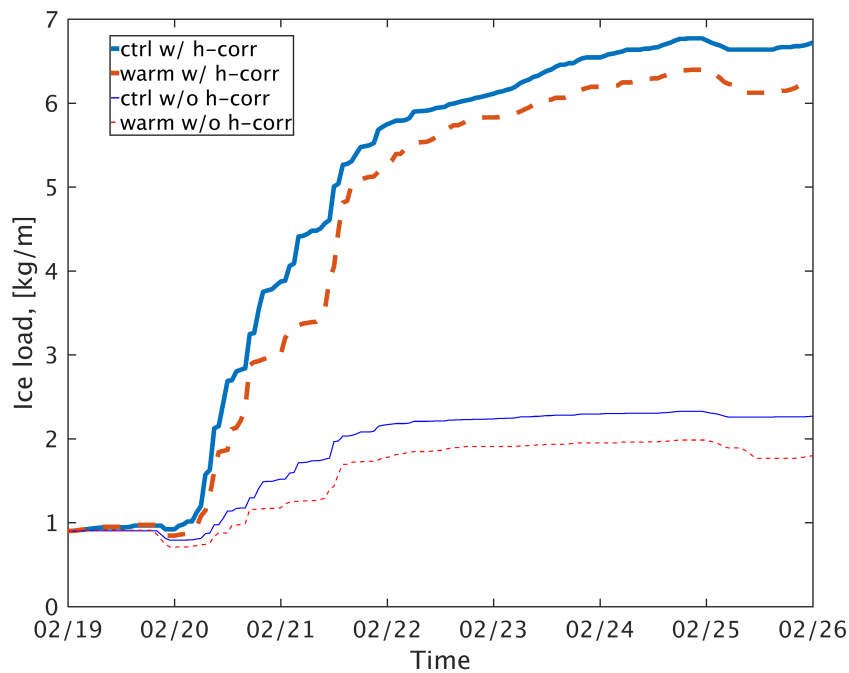


FIGURE 4.4: Comparison of absolute ice load differences between the warm run and control (short simulations) with and without height correction.

A control vs. warm run comparison of simulated ice loads both with and without height correction during the February 2016 Aalvik icing event is shown in Figure 4.4. With the exception of a short period around the 02/21 mark where there is a slightly greater difference between the height corrected curves (most likely due to larger icing object surface area), there is no indication of a substantial change in the absolute difference between the two simulations due to the 100m height difference between the model



and the real terrain. In this context, Figure 4.4 is only meant to illustrate that differences between control and warm run icing simulations without height correction can be assumed to be representative to icing differences in the real topography. Discussions regarding the actual icing differences between the two simulations are presented in Chapter 4.5.

Figure 4.5 shows accumulated ice loads calculated without any height correction from both short and long control runs for the same test case period. Although they are a good match initially, the two curves clearly separate at the beginning of the observed icing event. The reason for this must be a mismatch in the prediction of one (or more) variables included in the ice growth rate equation (equation 2.3) between the two simulations. A comparison of predicted temperature, cloud LWC and wind speed from both runs is shown in Figure 4.6 (temperature is not directly included in equation 2.3, however, it is an important factor in determining the accretion efficiency,  $\alpha_3$ ). The middle panel shows that there is clearly less LWC present in the long simulation at the time where the observed ice growth is most intense, resulting in less accumulated ice compared to the short run as shown in Figure 4.5. Again, it is important to point out that the Aalvik location was not affected by the smoothing of the model terrain (see Chapter 3.1.4).

The differences in simulated cloud LWC between the short and the long run could possibly be due to the extensive gap between the times of model initialization. At the beginning of the observed icing event, the long simulation has been running for over three and a half months, and is thus solely driven by boundary conditions as all information from the initial field is gone. The short run, however, was initialized only one day prior to the beginning of the icing event and is still to some extent characterized by the initial field.

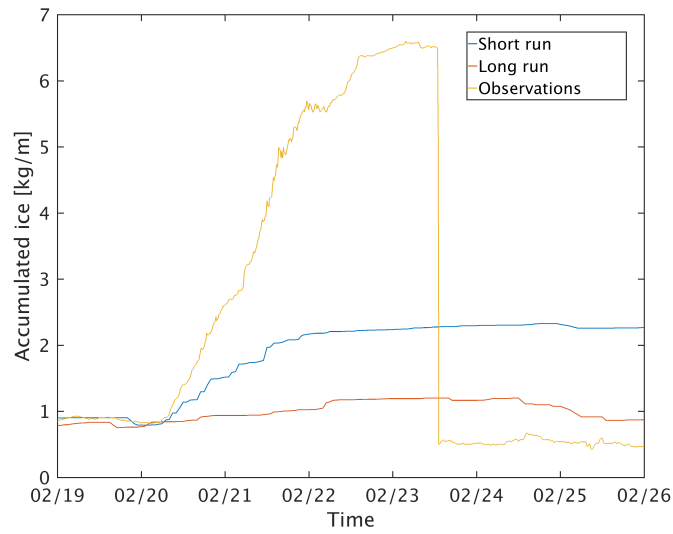


FIGURE 4.5: Short run vs. long run ice load comparison without height correction for the February 2016 Aalvik icing event.

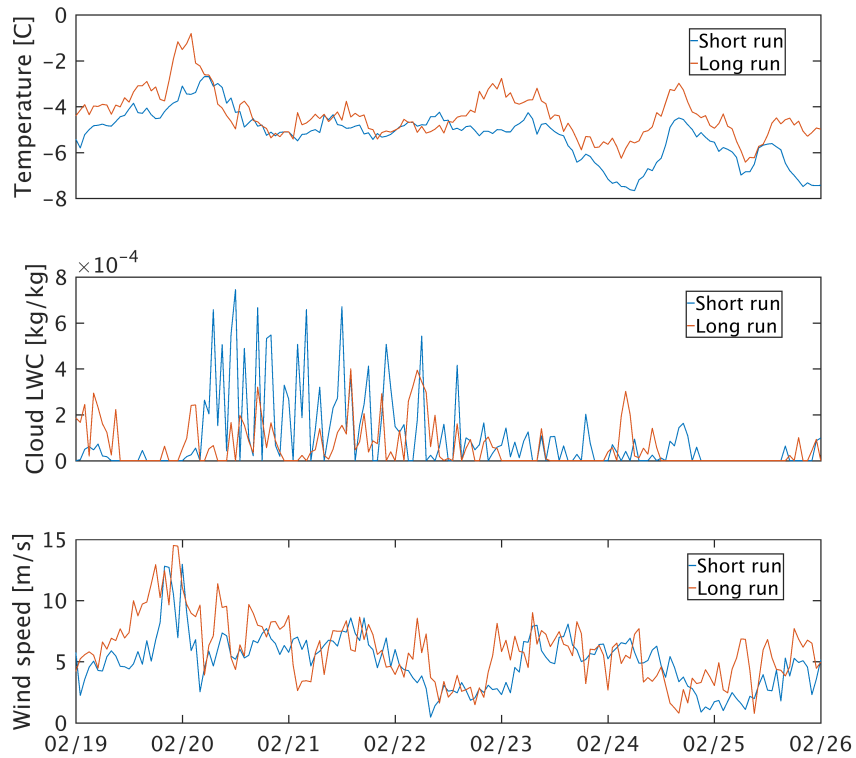


FIGURE 4.6: Short run vs. long run comparison of temperature (upper panel), cloud LWC (middle panel) and wind speed (lower panel) during the February 2016 Aalvik icing event.

## 4.2 Synoptic analysis of the February 2016 Aalvik icing event

So what type of large scale weather situation will typically lead to icing in South-West Norway? A quick look at the surface analysis (Figure 4.7) over the North Atlantic region reveals that a low pressure center located just east of Iceland was responsible for strong westerly winds impinging upon the south-west coast of Norway during the February 2016 Aalvik icing event. Large scale flow patterns similar to those shown in Figure 4.7 are fairly common in this region, and are typically seen during significant icing events both at Aalvik and in surrounding high altitude areas. Prolonged westerly airflow allows for continuous transport of moisture from the Atlantic Ocean towards the coast, where the air is orographically lifted. A large fraction of the available water vapor will then readily condense, leading to extensive precipitation along the coastline. The remaining moisture is advected further downstream, and continued lifting/cooling may produce clouds that come in contact with the higher grounds. If the temperatures here are below freezing, these clouds may contain rich amounts of super-cooled LWC yielding perfect conditions for in-cloud icing. In the presence of a low pressure system, significant icing events are most commonly observed during passages of warm- or occluded fronts, but also in the warm sector if the temperatures are not too high.

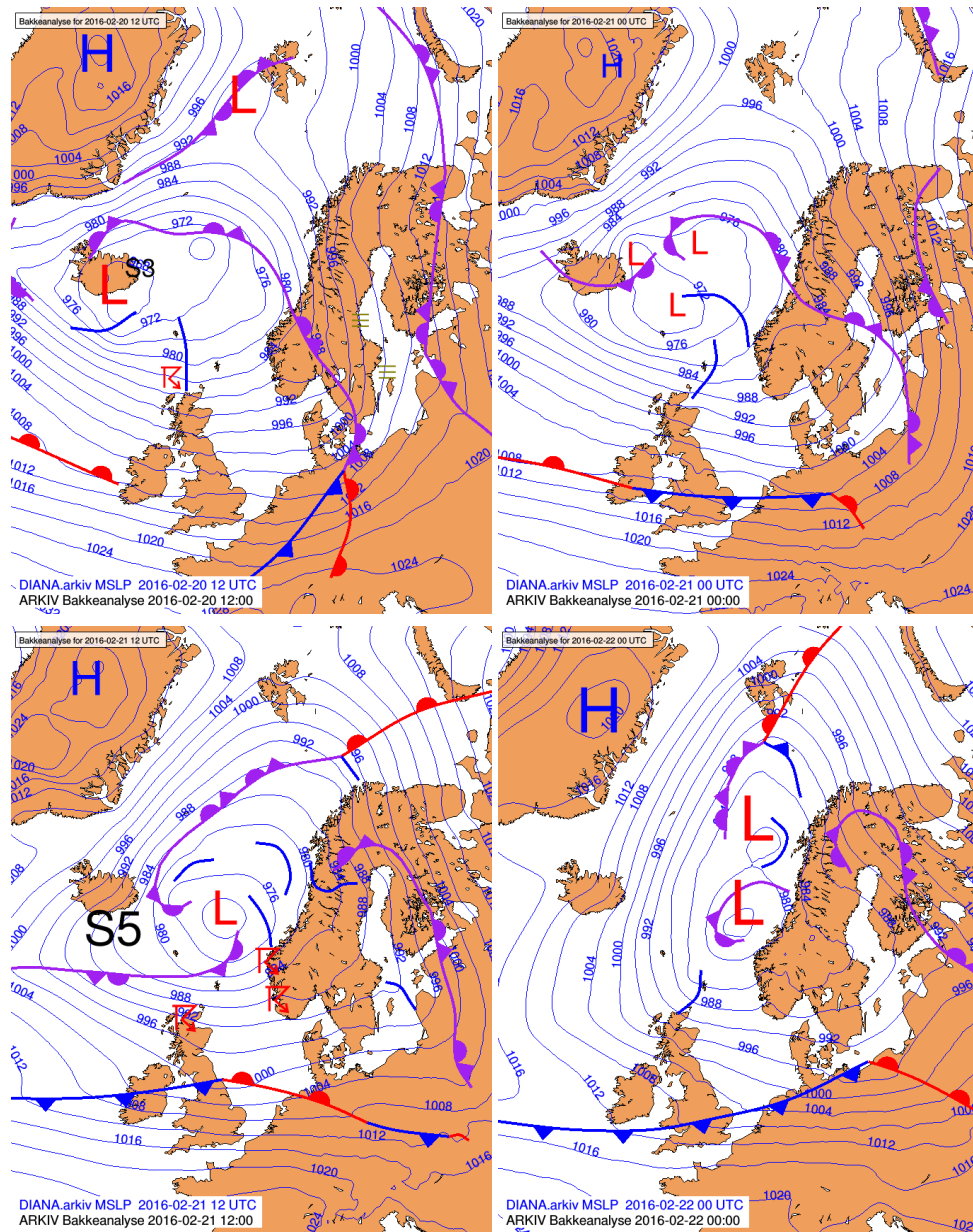


FIGURE 4.7: Surface analyses of the North Atlantic region during the February 2016 Aalvik icing event. A low pressure center just east of Iceland resulted in strong westerly winds across the south-west coast of Norway. The analyses are provided by the Norwegian Meteorological Institute.

### 4.3 Geographical distribution of icing

Utilizing the output from the full winter season control run, both accumulated ice load and *icing intensity* was calculated in every grid point of the innermost domain at all time steps. Icing intensity is the total amount of ice that accretes, in this case, on a standard object per unit of time, and is thus given in  $kg\ m^{-1}\ h^{-1}$ . As opposed to a growth rate obtained by taking the derivative of the accumulated ice load with respect to time, the icing intensity is independent of changes to the objects diameter ( $d=30mm$ ). The latter can therefore provide better information about the momentaneous icing response to the meteorological conditions at a given time, as the former will e.g. systematically be larger towards the end of an icing event if the surface area of the object has become sufficiently large.

Figures 4.8 and 4.9 show season maximum values of icing intensity and accumulated ice loads, respectively, across the innermost domain. It becomes evident from both figures that the exposure to extreme icing events in this region increases with terrain height. As can be seen from Figure 4.8, several of the highest mountain tops had maximum icing intensities approaching  $2\ kg\ m^{-1}\ h^{-1}$ , while the lower altitude regions in the western part of the domain all had maximum icing intensities well below  $1\ kg\ m^{-1}\ h^{-1}$ . However, not all icing events with high maximum icing intensities lead to extreme ice loads. In order for that to happen, conditions that enable ice accretion must persist for an extended period of time to allow for continual growth. In Figure 4.9, Folgefonna (the region of highest altitude, located around grid point (80,40) ) really stands out from the rest of the map, with maximum accumulated ice loads exceeding 160kg/m. Although several locations had maximum icing intensities matching (and even exceeding) the ones found at Folgefonna, the resulting ice loads were far less extreme. This could only mean that the most extreme icing events at said locations had considerably shorter durations than the ones at Folgefonna.

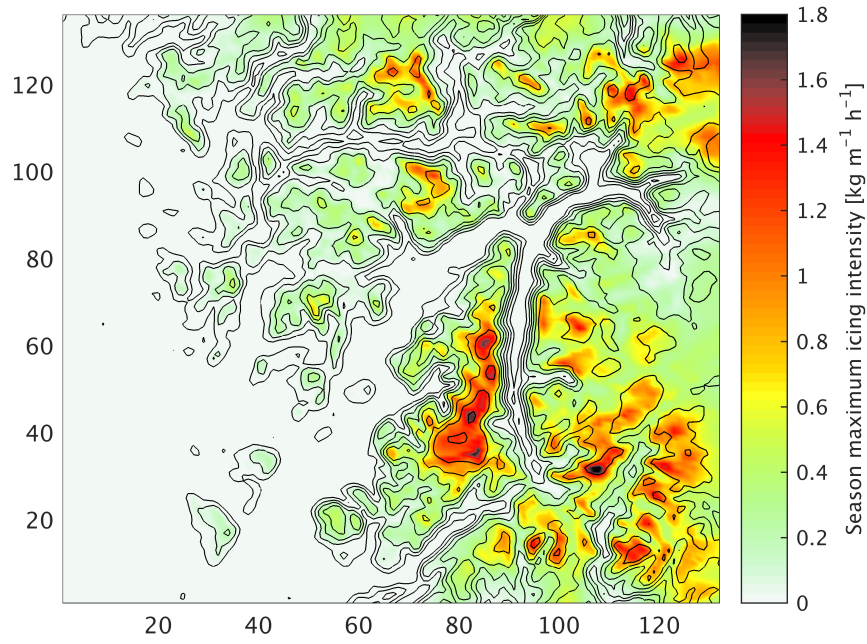


FIGURE 4.8: Season maximum icing intensities (long control run). Model grid points are on the x-y axis, and the black contours show model terrain height.

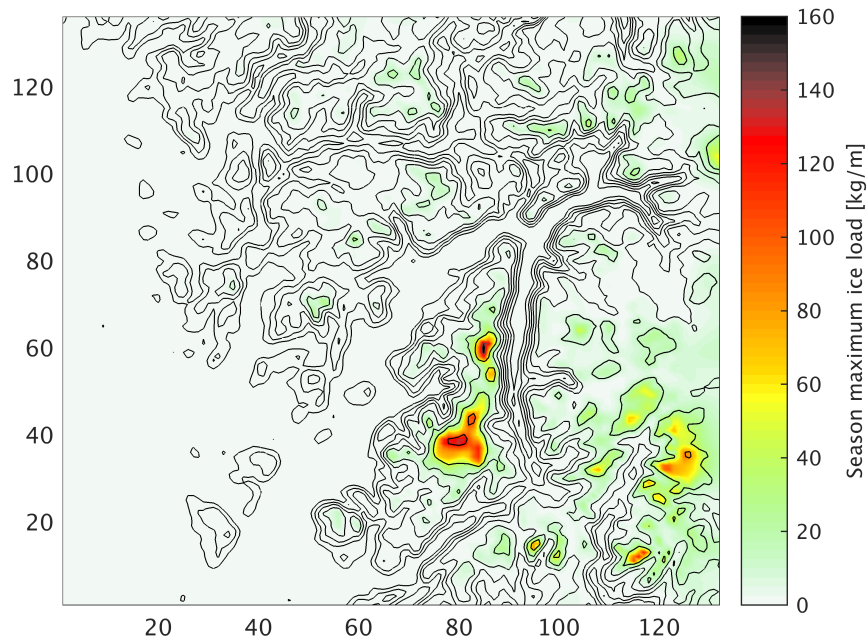


FIGURE 4.9: Season maximum accumulated ice loads (long control run). Model grid points are on the x-y axis, and the black contours show model terrain height.

#### 4.4 The effects of increased initial- and boundary temperatures on key icing related variables

So what happens when the temperatures in the initial field and at the model boundaries are increased by 2 °C? As described earlier, the relative humidity was not changed during the temperature modification which suggests that there should be additional consequences other than an overall increase in temperature. This section will address how the general meteorology reacts to the temperature change, including changes in humidity- and precipitation patterns as well as the temperature field itself - all of which are important to icing conditions.

Starting once again with the test case, Figure 4.10 shows plots of temperature, cloud water content and wind speed - all from the short, height corrected control- and warm simulations. Considering the 2 °C increase in initial- and boundary temperatures of the warm run, the resulting temperature time series shown in the upper panel is not very surprising. However, since the Aalvik location is not close to any model boundary, the temperature difference between the two runs is not uniformly at 2 °C throughout the entire period, but ranges from 0.95-2.56 °C. Note also that both temperature profiles stay well below the freezing point during the entire period.

As can be seen from the middle panel, both runs produced substantial amounts of cloud LWC. Shorter periods can be found where the warm run has higher cloud LWC than the control, and vice versa. However, no significant difference in cloud LWC between the warm run and control was found when taking the average over the 7 day period. The impacts of increased temperatures on cloud LWC are discussed in further detail in sections 4.4.1 and 4.5.1, where data from the long simulations are reviewed. Out of the three variables plotted in Figure 4.10, the wind speed seems to be the one that was least affected by the temperature change. Only a few sporadic events with higher winds in the control run can be seen, with a maximum difference of 6.5m/s.



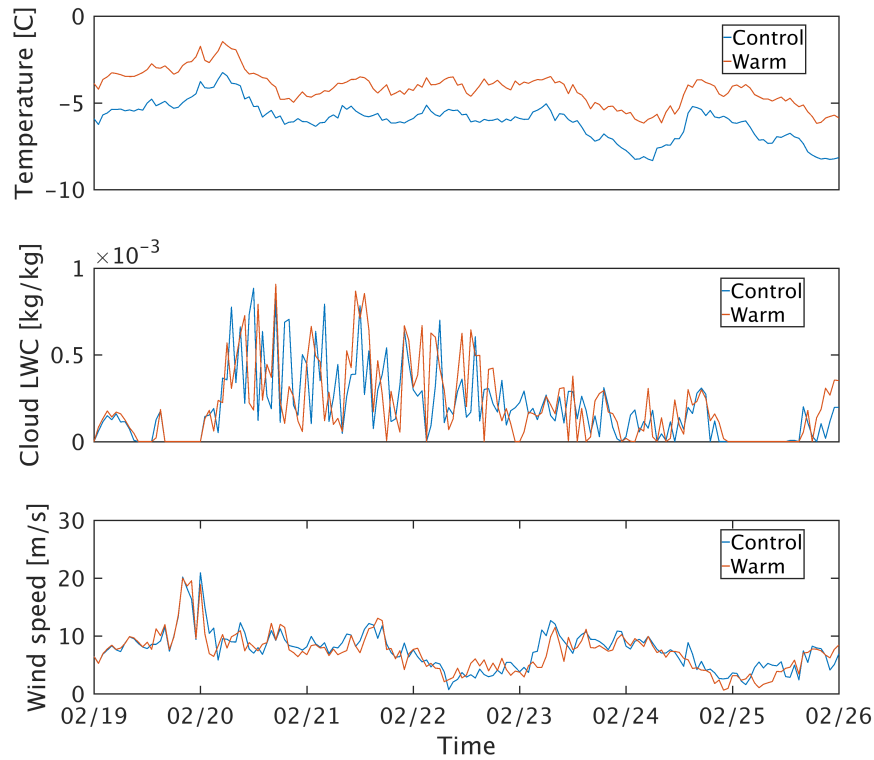


FIGURE 4.10: Control run vs. warm run comparison of temperature (upper panel), cloud LWC (middle panel) and wind speed (lower panel) for the February 2016 Aalvik icing event.

The results from the test case shown above is only one example of how important icing-related variables may change due to increased temperatures. In order to get a broader picture of how these variables react, results from the full winter season simulations will be presented next.

Figure 4.11 shows the difference in season mean temperature between the warm run and the control over the entire innermost domain (note that the temperature change was made at the boundaries of the parent (outermost) domain only, hence the temperature difference at the boundaries of the innermost domain is not prescribed as can be seen in Figure 4.11). Although the season mean temperature difference only slightly differs from  $2^{\circ}\text{C}$  across the domain, it has a tendency to increase with terrain height. The lion's share of the domain has a season mean difference of slightly less than  $2^{\circ}\text{C}$ , except at the highest mountain tops in the south-east region of the domain where it barely exceeds  $2^{\circ}\text{C}$  (discussed in next section). The season average wind speed difference between the two runs is shown in Figure 4.12. Although the difference is close to zero across the domain, high altitude regions once again stand out as the most affected areas.



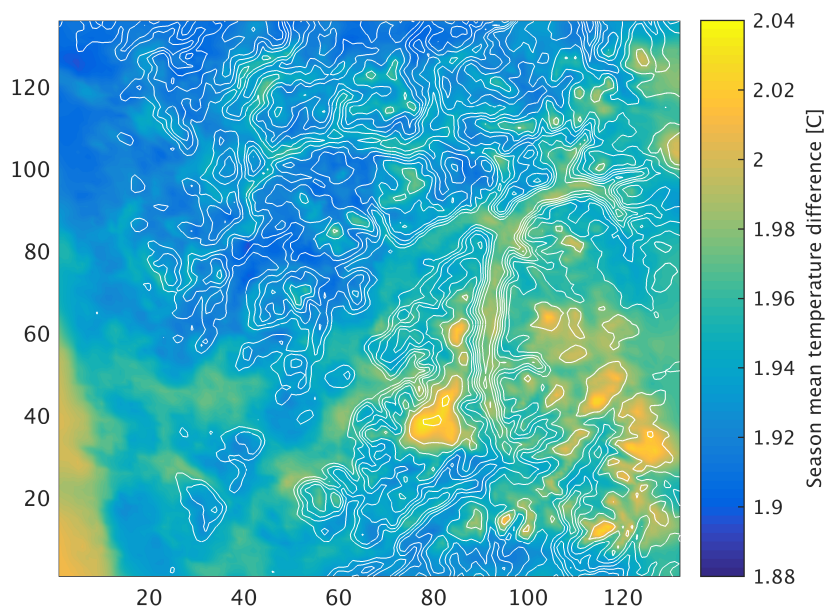


FIGURE 4.11: Difference (warm-control) in season mean temperatures at the lowest vertical model level. Model grid points are on the x-y axis, and the white contours show model terrain height.

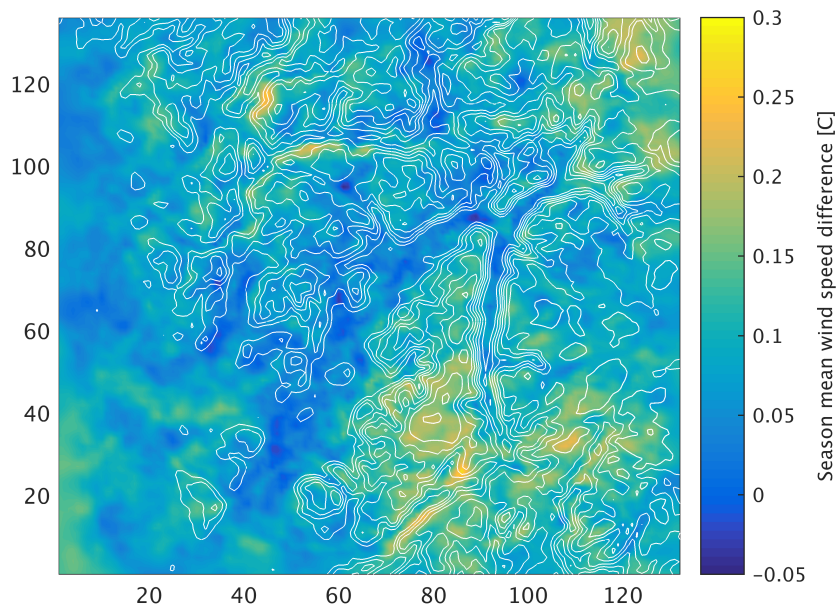


FIGURE 4.12: Difference (warm-control) in season mean wind speeds at the lowest vertical model level. Model grid points are on the x-y axis, and the white contours show model terrain height.

#### 4.4.1 Changes to humidity conditions and precipitation patterns

Consistent with the theory described in chapter 2.3, Figure 4.13 shows that the warm run indeed has higher specific humidity on average than the control. The differences seem to be greatest at low altitudes, with a high density of points between 0.6-0.7 g/kg at elevations lower than 200m. It was also stated in Chapter 2.3 that because the saturation water vapor pressure increases exponentially with temperature, a warm air parcel would have a higher increase in specific humidity than a colder counterpart during a temperature increase at constant relative humidity. This explains why the specific humidity differences are largest at low altitudes, as temperature generally decreases with height.

Figure 4.13 may also partially explain why the temperature differences between the control and the warm run seemed to be greatest in high altitude regions (see Figure 4.11). Due to the added moisture in the warm run, more water will condense into the air parcels as they are orographically lifted by the steep terrain, leading to an amplification of latent heat release.

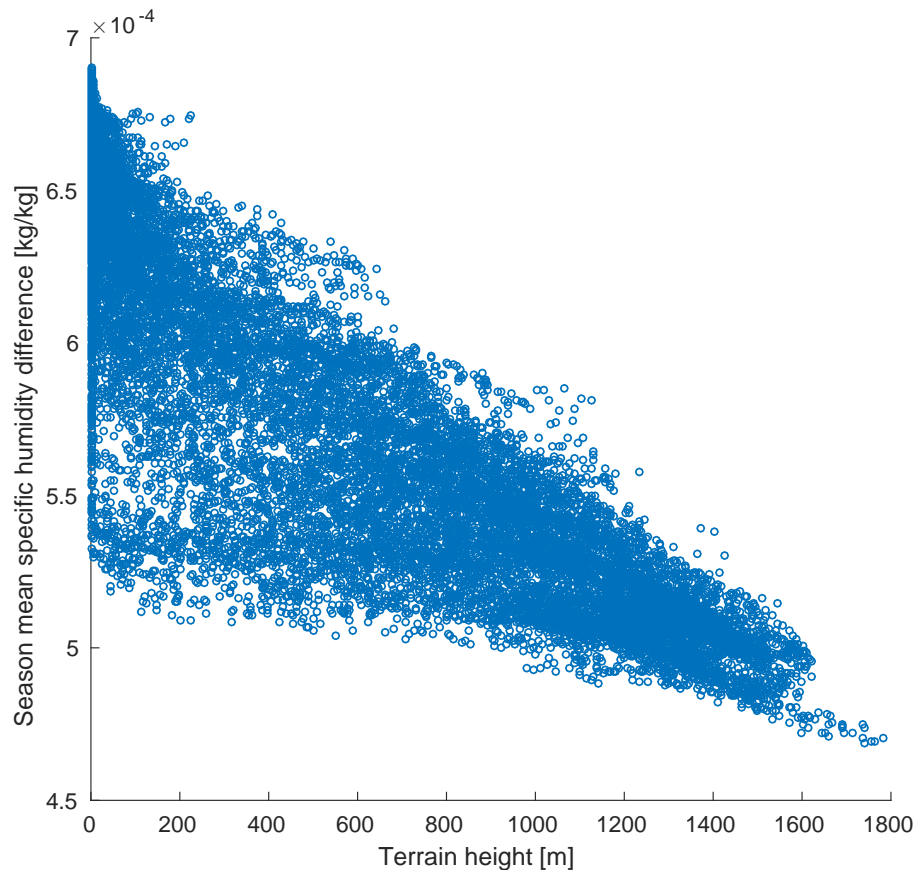


FIGURE 4.13: Total season mean difference (warm-control) in water vapor mixing ratio vs. terrain height. Each point represents one model grid point, and all values are from the lowest model layer only.

Although Figure 4.13 indicates that the method worked the way it was intended to, it does not necessarily give any insight into how the temperature increase may have altered the icing conditions. Since the rate of ice growth by deposition of water vapor (hoar frost) is negligible compared to that of water particles colliding with the icing object (see chapter 2.2), the added water vapor in the warm run must first undergo a phase transition in order for it to have a notable impact on the icing conditions. In this regard, it is necessary to investigate how the extra moisture affected the abundance of cloud LWC in the warm run. Furthermore, a look at possible changes in precipitation patterns may help to understand how the added moisture was distributed across the domain.

### Precipitation

With westerly winds dominating the airflow along the western coast of Norway, where mountains are standing in line to provide lifting, the area covered by the model domain in this study is frequently subjected to orographically induced precipitation, and is among the wettest parts of the country (Tveito, 2010).

Figure 4.14 shows the difference in total accumulated precipitation (rain + snow) between the warm run and control. In the south and south-west parts of the domain, over the ocean and along the coast, the warm run has an overall increase in accumulated precipitation with a maximum of about 600mm around Folgefonna. The most striking feature of Figure 4.14 on the other hand, is perhaps that over quite a large region in the north-east part of the domain, the warm run actually has less accumulated precipitation than the control with reductions as high as -400mm in some areas. Similar maps where accumulated rain and snow are plotted separately reveals that in these areas, the control has considerably more precipitation in the form of snow than the warm run, whereas the difference in accumulated rain is close to zero.

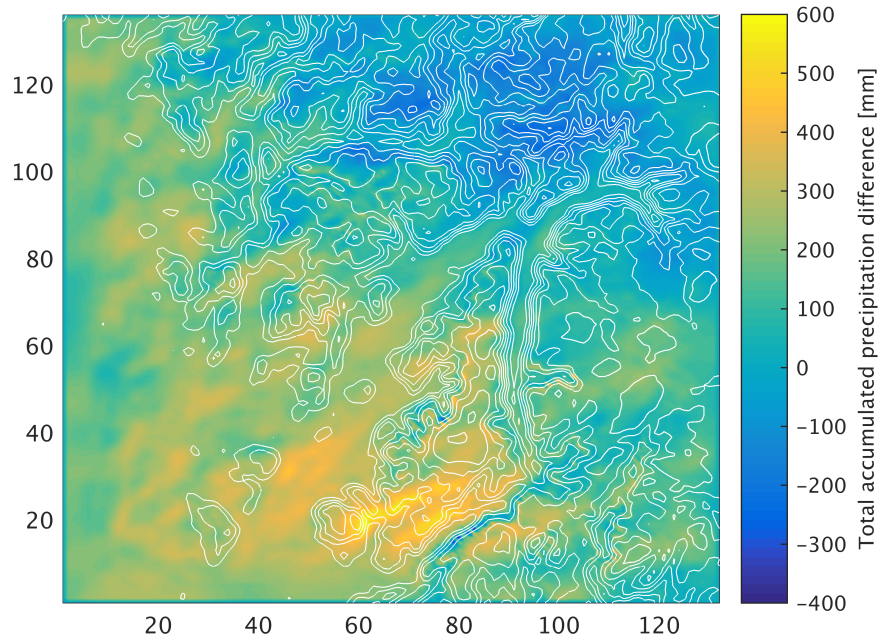


FIGURE 4.14: Difference (warm -control) in total accumulated precipitation (rain + snow) for all five months. Model grid points are on the x- and y axes, and the white contours show model terrain height.

Considering that the airflow is dominated by westerly winds, Figure 4.14 suggests that a substantial fraction of the extra moisture in the warm run was removed upstream of the most icing exposed regions (Figure 4.9) due to precipitation. The fact that the area of maximum precipitation moved upstream due to the temperature increase could partially be explained by a shift of precipitation type from snow to rain. Higher temperatures will cause more precipitation to fall as rain, and because the fall speed of a rain-drop is higher than that of a snow particle, the latter will be advected further downstream before reaching the ground. This particular phenomenon was addressed in a numerical study by Pavelsky et al. (2012), and the results showed similar patterns to those in Figure 4.14.

#### Cloud liquid water content

So what about the key driver of atmospheric icing, namely the cloud liquid water content (LWC)? Figure 4.15 shows the difference in season mean cloud LWC between the warm run and the control (positive values mean higher LWC in the warm run, and vice versa) at the lowest vertical model level. Even more so than the temperature difference (Figure 4.11), the magnitude of the LWC difference shows a clear dependency on terrain height. A curious thing to notice though, is the apparent change of *sign* going from



west to east. While the high altitude regions in the eastern part of the domain have higher LWC (positive values) in the warm run, the situation is exactly the opposite in the west (the difference here is smaller, but so is the altitude). Areas directly above the ocean seem to be relatively unaffected with regards to this matter.

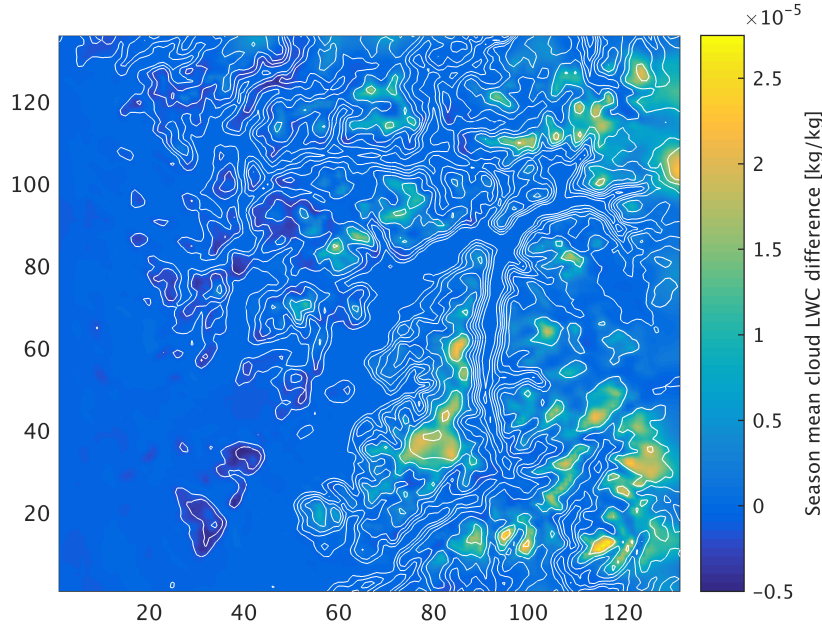


FIGURE 4.15: Difference (warm-control) in season mean cloud liquid water content (LWC) between warm run and control. All values are from the lowest vertical model level only. Model grid points are on the x- and y axes, and the white contours show terrain height.

## 4.5 Control vs. warm run icing

We saw in the previous section that the increased initial- and boundary temperatures inflicted changes to key ingredients in equation 2.3, which yields the growth rate of ice on a standard icing object. In particular, the warm run had higher season average values of LWC in the highest altitude regions, in addition to the obvious higher temperatures across the domain. This section provides figures showing how these differences impacted the calculated ice growth in the ice accretion model (see chapter 3.1.5), including seasonal averages and extreme value analyses.

Starting once again with the test case, Figure 4.16 shows a control vs. warm run comparison of accumulated ice load calculations. Both calculations have been vertically interpolated to match the true height of the Aalvik station as described in chapter 3.1.5. Although the two curves are quite similar, there is more accumulated ice in the control run at all times

after the icing event starts around the 02/20 mark, with a maximum difference of 1.1kg/m. Remembering Figure 4.10, the temperature in both runs stays below freezing during the entire period, hence there is no melting in either case <sup>1</sup>. From that same figure we also saw that the two simulations alternated in having the highest content of liquid water during the icing event. It is also clear from Figure 4.16 that the ice growth rate is sporadically larger in the warm run, even though the accumulated ice load never exceeds that of the control run.

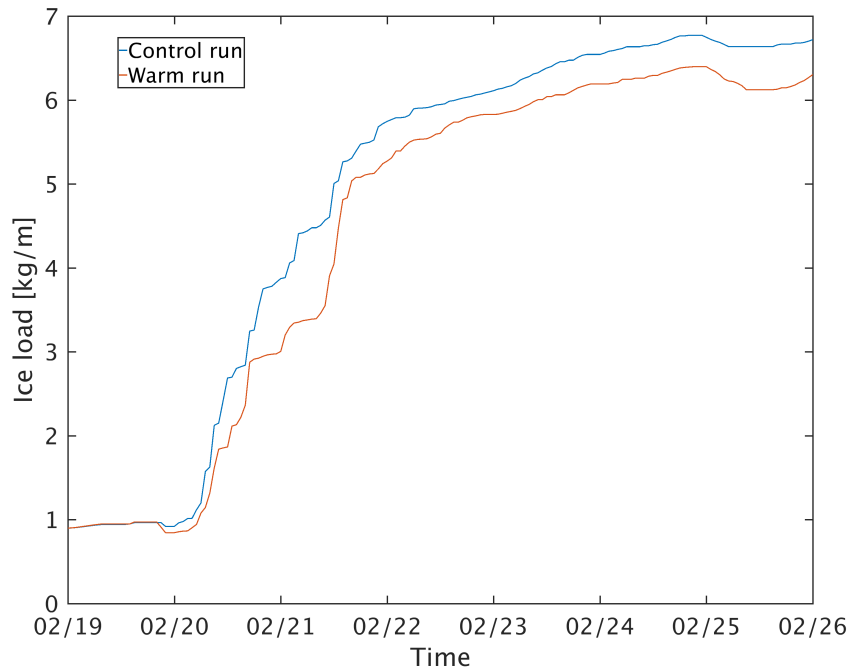


FIGURE 4.16: Control vs. warm run comparison of accumulated ice for the February 2016 Aalvik icing event (short simulations). Both curves are height corrected.

Before moving on to the main results of this study, let us do a quick summary of what we have seen so far: The test case showed that the ice accretion model was able to recreate the observed icing event at Aalvik rather well, and the warm run had slightly less accumulated ice compared to the control. From Figure 4.9 and 4.8 we saw how the season averages of maximum ice loads and icing intensities increased with terrain height in the control run. It also became evident from Figure 4.14 that a substantial fraction of the extra moisture in the warm run was removed upstream of the most icing exposed regions due to enhanced precipitation. The control vs. warm run comparisons of the key icing variables (LWC and wind speed) in Chapter 4.4 both showed similar tendencies; the differences between the

<sup>1</sup>In some cases, melting can occur in the ice accretion model even if the temperature of the environment is below freezing. If the heat balance in equation 2.2 is positive, i.e. the heating terms are larger than the freezing terms,  $\alpha_3$  is set to zero.

two simulations seemed to be amplified in high altitude regions, where the warm run had higher LWC as well as slightly stronger winds averaged over the winter, both of which could count towards more icing in the warm run. However, this is where the average temperature differences were largest as well, exceeding the  $2^{\circ}\text{C}$  limit only at the highest mountain tops. So which one of these opposing effects will dominate, and possibly cause an icing difference?

Figure 4.17 shows differences in season mean accumulated ice loads between the warm run and the control. Notice that there are no positive values, meaning that in not a single grid point, the warm run had higher accumulated ice loads than the control, averaged over the winter season. Once again, Folgefonna stands out as it completely overshadows the surrounding areas with massive differences of around  $50\text{kg/m}$ . Furthermore, the control run also had greater season maximum ice loads across the domain when compared to the warm run (not shown).

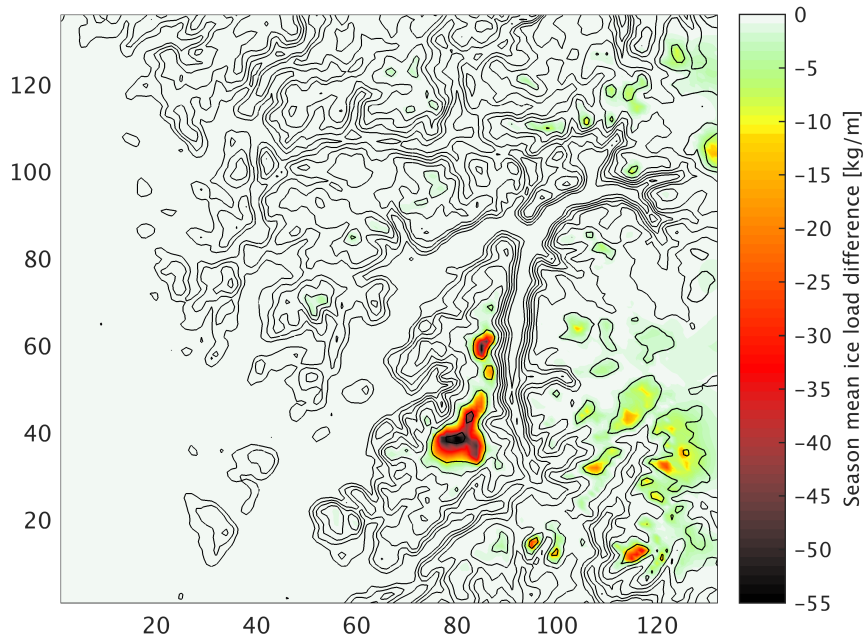


FIGURE 4.17: Differences (warm-control) in season mean ice loads. Model grid points are on the x- and y axes, and the black contours show model terrain height.

Even though the warm run had an overall reduction in icing, sporadic events can be found where both accumulated ice and icing intensity exceed those of the control. In fact, as can be seen from Figure 4.18, there are a few locations where the maximum icing intensities were higher in the warm run. However, by examining time series of ice accumulation at various locations, episodes with more icing in the warm run than in the control are

found to be quite rare and often have very short durations. Nevertheless, the blue areas in Figure 4.18 indicate that there at least is a potential for enhanced icing events in the warm run.

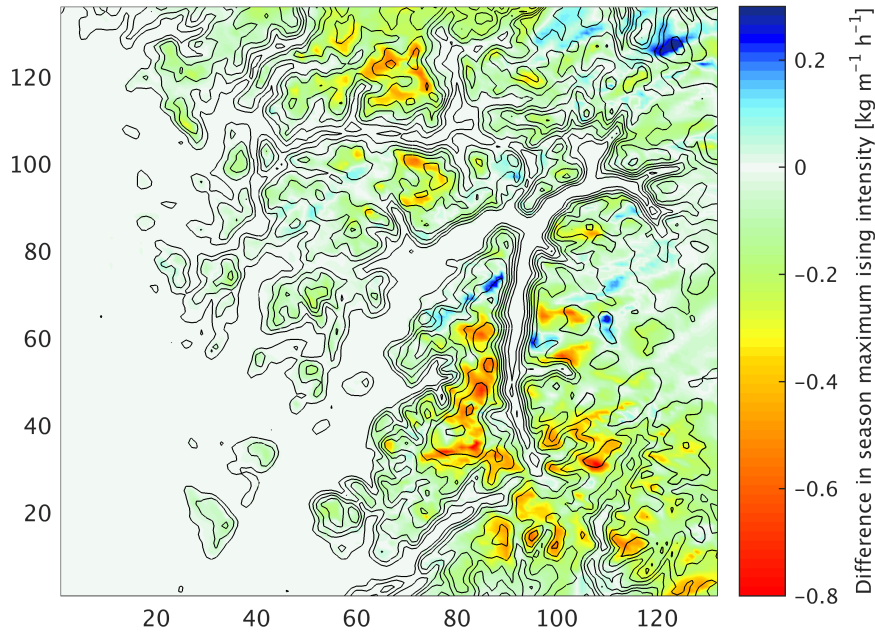


FIGURE 4.18: Differences (warm-control) in season maximum icing intensities. Model grid points are on the x- and y axes, and the black contours show model terrain height.

#### 4.5.1 Terrain height dependency

It has become evident from the results so far that the differences between the two simulations escalate with increasing terrain height. However, the details of these height dependencies might be hard to identify based solely upon the type of maps presented in the previous section. In order to get a better understanding of this particular issue, differences in season average cloud LWC and accumulated ice loads are plotted against terrain height in Figures 4.19 and 4.21, respectively.

Although the differences in LWC averaged over the season are on the order of  $10^{-5}$  kg/kg, there is a clear trend in Figure 4.19. Starting at around 800m, the two simulations seem to diverge steadily with increasing altitude, reaching a maximum difference at around 1600m. Notice also that between 200m and 800m there is a slight predominance of negative values, meaning that in several locations within this height interval there was higher LWC in the control compared to the warm run averaged over the season. This also became apparent from Figure 4.15, where the control had higher LWC in the higher altitude areas in the western part of the domain.



Figure 4.20 shows the differences in percentages and might give a clearer picture of how significant the increased LWC of the warm run is at the highest altitudes. We see that around 800m, the median is crossing the 0% line and becomes increasingly positive with altitude. At around 1450m the median exceeds 10%, meaning that at least 50% of the grid points at this altitude or higher have at least 10% higher LWC in the warm run compared to the control on average. Again, all values of cloud LWC are from the lowest vertical model level only.

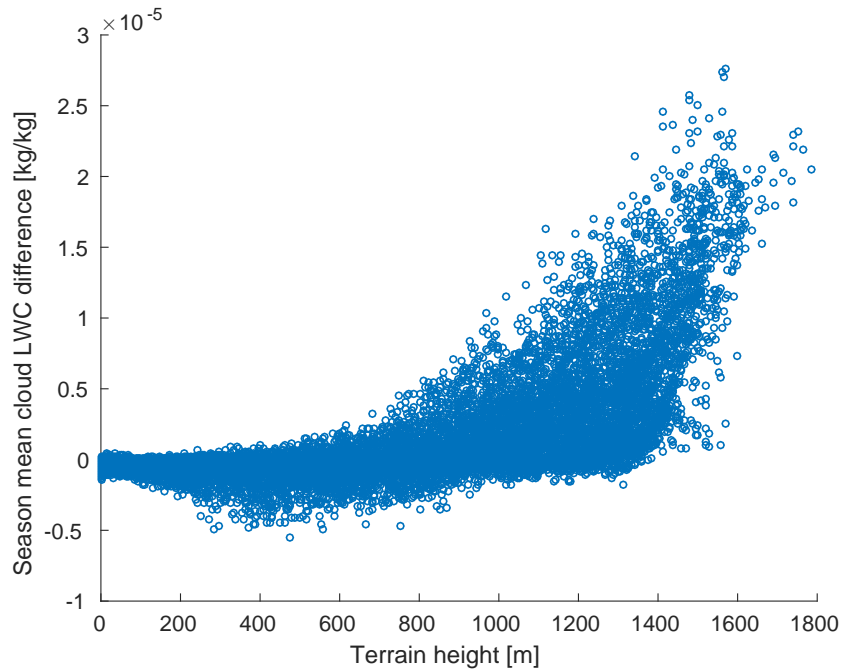


FIGURE 4.19: Differences (warm-control) in season average cloud LWC vs. terrain height. Each dot represents one grid point, and all values are from the lowest vertical model level only.

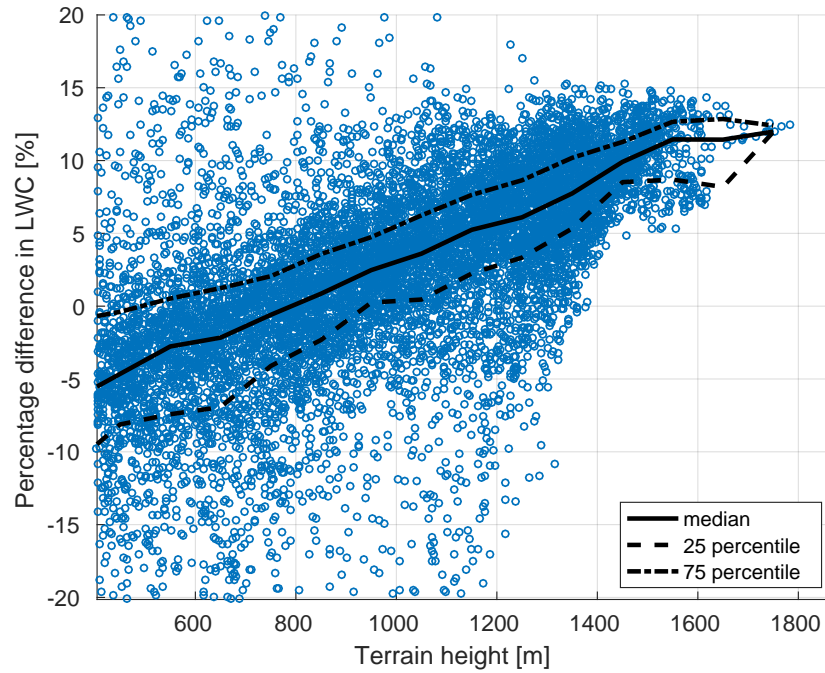


FIGURE 4.20: Percentage difference (warm-control) in season average cloud LWC vs. terrain height. Each dot represents one grid point, and all values are from the lowest vertical model layer only.

What we literally saw the contours of in Figure 4.17, and which becomes even clearer from Figure 4.21, is that the average difference in accumulated ice loads vs. terrain height has quite the opposite trend than that of the difference in season average cloud LWC. With little to no difference at altitudes of 900m or less, the difference between the two simulations becomes rapidly more negative with increasing height above the lowest kilometer, with a maximum difference approaching  $-60\text{kg/m}$  at around 1600m. Although the magnitude of the differences in both LWC and accumulated ice loads seems to have a slight dip in the uppermost 200m, there are very few points at this altitude and the dip could just as well be due to other factors such as geographical location.

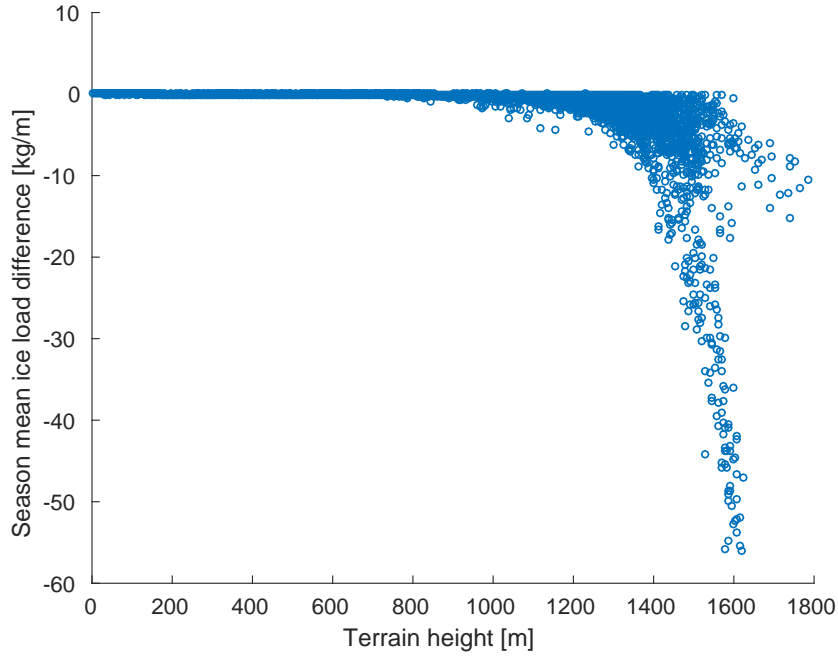


FIGURE 4.21: Differences (warm-control) in season average ice loads vs. terrain height. Each dot represents one grid point.

#### 4.5.2 Change in occurrence frequency of icing events

Even though we have seen that the warm run had an overall decrease in both season average- and maximum ice loads, it could be useful to get a clearer picture of the change in occurrence frequency of icing events with ice loads of various degrees. For instance, power lines installed in icing exposed regions are often designed to withstand maximum ice loads with estimated return periods that are reasonable with respect to the desired lifetime of the power line. However, it is not only the sheer weight of the ice that decides the harmfulness of an icing event. Prolonged and frequent icing events of lesser magnitude can cause structural fatigue over time, and heavy ice loads in combination with strong winds can be particularly devastating.

Mapping out and comparing every icing event, by assessing both maximum ice load and duration, across the domain for the extent of the entire season would be a very cumbersome process. Even more so if one was to include the aspect of ice loads in combination with wind speeds. However, by counting and comparing the total amount of occurrences, in both time and space, where the ice load is within a certain interval, one could (hopefully) get a better grasp of how the risk of potentially harmful icing events changed due to the increased temperatures.

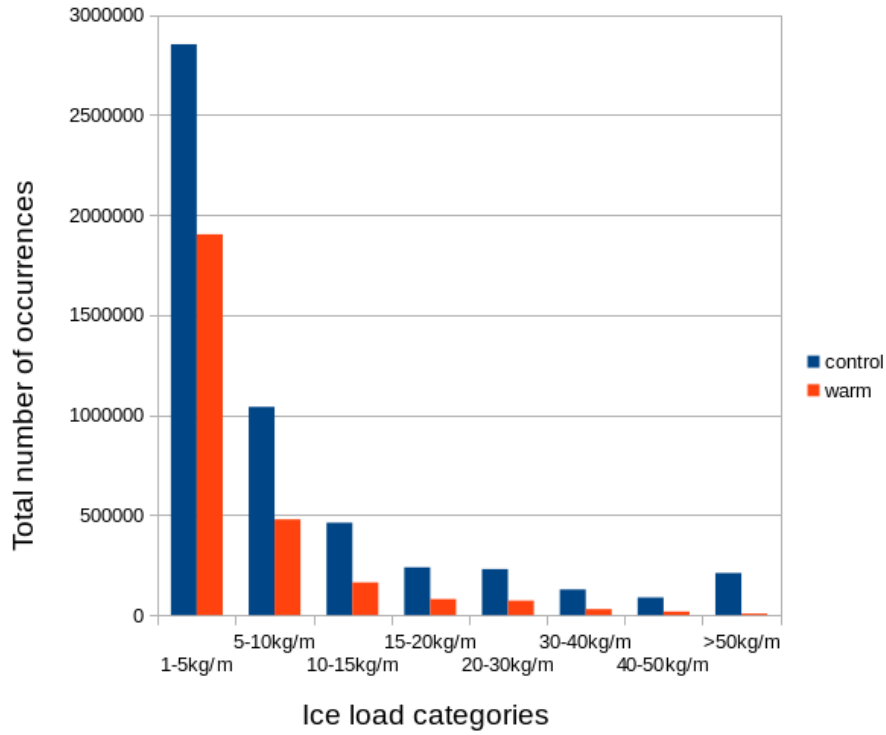


FIGURE 4.22: Total number of occurrences, in both time and space, of icing events within different ice load categories from the long control and warm simulations.

The quantity on the y-axis of Figure 4.22 is admittedly somewhat peculiar, and could probably use some further explanation. As mentioned earlier, accumulated ice loads were calculated hourly throughout the season in every grid point. Hence, if a certain ice load was calculated in grid point  $(i,j)$  at  $t = t_k$ , it would count as one occurrence in the respective ice load category in Figure 4.22. Should the ice load in the same grid point at  $t = t_{k+1}$  stay within the same category, it would count as another occurrence and so on. Another thing to be aware of in Figure 4.22, is that the intervals constituting the different ice load categories are not equally large. In particular, the rightmost category covers all ice loads that are 50kg/m or higher.

So what does Figure 4.22 tell us? First of all, the overall number of occurrences in both simulations naturally drops with increasingly extreme ice loads. Secondly, the control has a significantly higher number of occurrences in every category than the warm run. Consequently, if e.g. a power line designed to withstand ice loads up to a certain threshold was randomly placed within the domain, the occurrence probability of an icing event with ice loads exceeding that threshold would be higher in the control run. Also, the relative difference between the two simulations seems to be largest in cases of extreme ice loads, particularly in the >50kg/m category.



## Chapter 5

# Discussion and conclusions

The objective of this study was to address how icing conditions in western Norway might change in a future climate with higher temperatures and atmospheric moisture. Other possible impacts of climate change were not taken into account, and the results that were presented must therefore not be interpreted as an attempt to portray what the overall icing conditions will look like by the end of the 21st century. Rather, they aim to explain how increased temperatures and specific humidities may affect icing in a future winter with general atmospheric flow patterns that are similar to those of the present climate. A complete prediction of future icing conditions would require every aspect of climate change to be accounted for, and could better be obtained e.g. by forcing the numerical weather prediction model with output from climate models. There are, however, indications that the results of this study could still provide valuable information about the impacts of global warming on the local icing conditions, despite not having taken into account all aspects of climate change.

In the Fifth Assessment Report, the Intergovernmental Panel on Climate Change (2014b) reviews the latest progress in long term climate change projections and the subsequent changes to large scale atmospheric circulation patterns. Although the jets are estimated to shift about 1° poleward in the northern hemisphere, indications of changes to the extratropical storm tracks are small and uncertain, particularly over the North Atlantic basin. Based on this review, it seems unlikely that the airflow over the western coast of Norway will be radically different from what it is today, and that similar large scale weather situations to those that are typical in today's climate will not be seen come the end of the 21st century. The results presented in this study could therefore prove useful in generally describing how the production of precipitation and cloud LWC by orographic lifting may change in the coastal region of western Norway due to global warming, and how this could further affect icing conditions.

## 5.1 What made the difference?

The underlying hypothesis of this study was that the warm run, having higher specific humidity at saturation, would produce clouds with increased LWC that eventually could lead to more intense icing events, at least in some cases. As can be seen from Figures 4.15 and 4.19, the warm run did indeed produce average levels of LWC surpassing those of the control, particularly in high altitude regions. However, Figure 4.21 clearly depicts that this did not lead to greater season average ice loads in those regions. Rather, it shows quite the opposite. When comparing Figures 4.19 and 4.21 showing differences in season mean LWC and accumulated ice loads plotted against terrain height, it is almost as if they are mirrored about the height-axis. In other words, the altitudinal regions where the accumulated ice loads in the warm run falls shortest in comparison with the control are the same regions where differences in cloud LWC are most prominent (with the warm run having larger values). So what made the difference?

### 5.1.1 Temperature

By closely examining time series of the key variables in the ice growth equation at specific locations, it becomes evident that the temperature increase by itself made the biggest difference in most cases. For example, by the end of the 12 day long icing event at Folgefonna shown in Figure 5.1, the control has an accumulated ice load that is close to 80kg/m greater than that of the warm run, with both runs having no ice at the beginning of the event. In addition to accumulated ice loads, the figure also shows time series of temperature, LWC and wind speed from both simulations. Although there are sporadic periods where the control has higher LWC and/or stronger winds, it is hard to argue that the massive ice load differences in this particular case are due to the relatively minor differences in either one of them. In fact, the control has slightly less cloud LWC than the warm run averaged over the 12 day period. Furthermore, no periods can be seen in which the control has strong winds - while the warm run does not.

The circles in the second panel of Figure 5.1 highlights three decisive periods where the higher temperatures of the warm run has significant consequences for the resulting ice accumulation. As strong winds and rich amounts of LWC are both present, once the temperature in the control sinks below 0°C (dashed line) within the leftmost circle, ice immediately starts to grow as depicted by the blue curve in the top panel. In the warm run, however, the temperature stays above freezing for a little while longer, allowing the control to have a notable head start with respect to ice accumulation. Within the middle circle, the warm run temperature rises above the 0°C line, while the temperature of the control remains below by a hair's

breadth. As can be seen from the top panel, this small, yet critical temperature difference is causing further divergence between the two ice load curves. While the ice is allowed to grow steadily in the control, the warm run has nearly all it's ice melted away. A similar situation is found in the period within the righthmost circle.

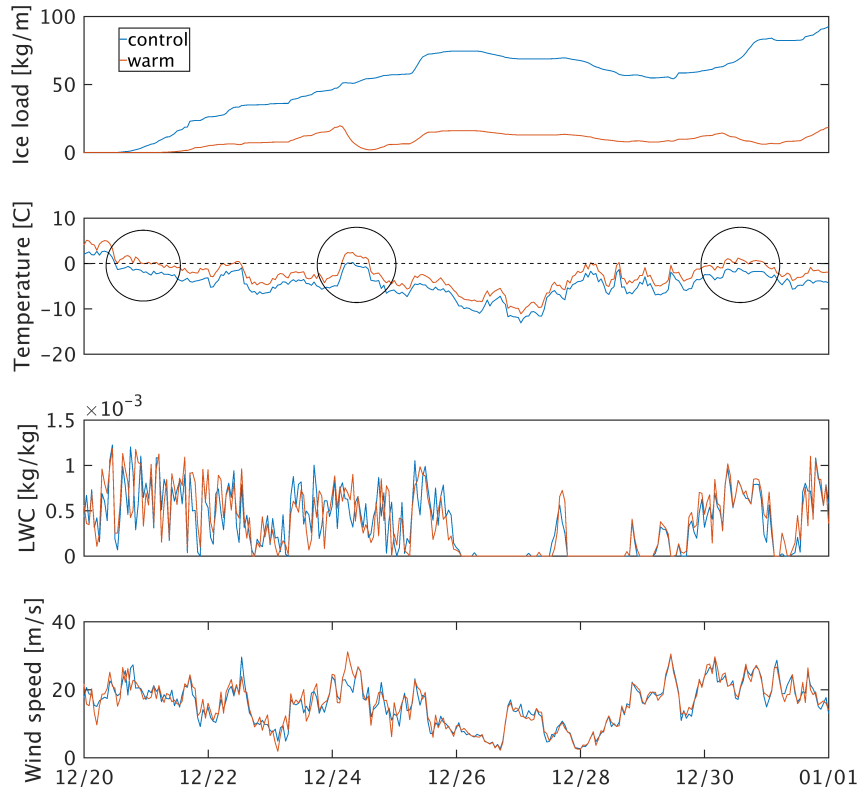


FIGURE 5.1: Warm run vs. control comparisons of ice load (upper panel), temperature (second panel), cloud LWC (third panel) and wind speed (lower panel) for the December 2015 Folgefonna icing event. All values are from the lowest model level.

Another thing to bear in mind: as long as the temperature is below freezing, and there is a sufficient presens of large water particles and wind, the ice accretion model will produce ice. However, even in a stricly sub-zero regime the growth rate is still dependent on temperature. As described in chapter 2.2, the accretion efficiency,  $\alpha_3$ , in equation 2.3 is reduced from unity in the case of wet growth, i.e. when there is a liquid water layer on the surface of the icing object. This suggests that  $\alpha_3$  is consistently smaller in the warm run compared to the control, unless the temperature in *both* runs is sufficiently low to have dry growth conditions (in which case  $\alpha_3 = 1$ ).



Considering the above discussion, questions as to what may have happened with the warm run icing had it not been for the extra melting episodes naturally arise. As Folgefonna is within the altitudinal region where the median of the percentage difference in cloud LWC approached 10% (Figure 4.20), persistent sub-zero temperatures during similar events could potentially lead to more icing in the warm run. To further investigate this possibility, the cloud LWC of the control run was increased by 10% and icing calculations were performed over again with the IAM for the same event that was discussed above. The results are shown in Figure 5.2, and the added LWC did indeed lead to greater ice loads as can be seen from the upper panel. The lower panel shows that the added LWC caused numerous spikes of amplified icing intensities, resulting in 7.6kg/m more accumulated ice by the end of the 12 day period.

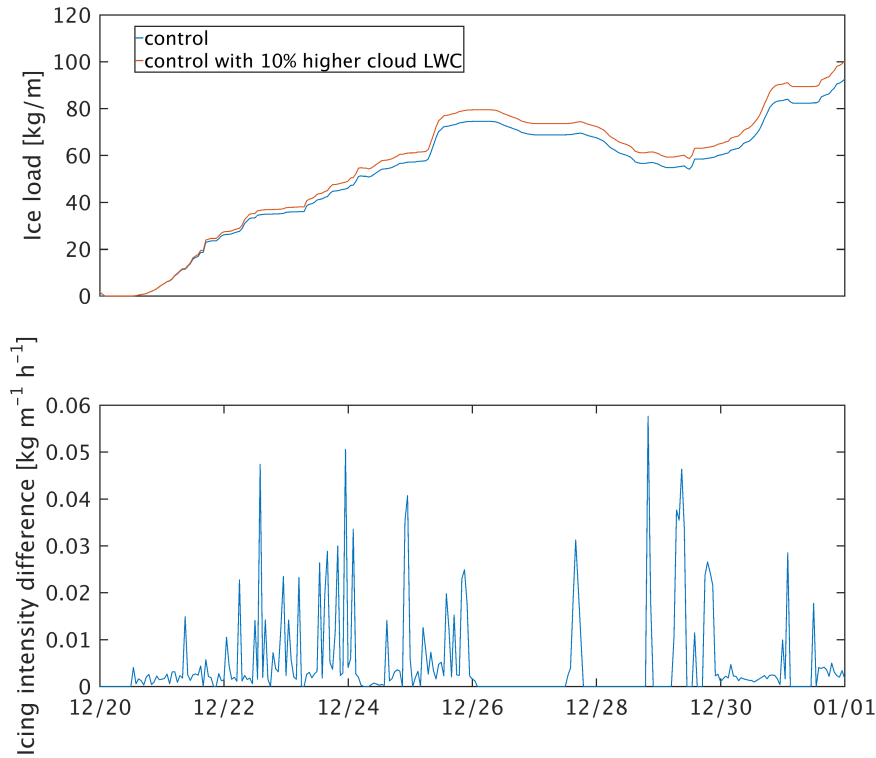


FIGURE 5.2: Upper panel: Accumulated ice loads from control run with 10% higher cloud LWC (red curve) for the December 2015 Folgefonna icing event. The blue curve is the same as the blue curve in the upper panel of Figure 5.1. Lower panel: Icing intensity differences between the curves of the upper panel (red-blue).

## 5.2 Future research

As pointed out in the discussion above, situations where the temperature of the control run was just below freezing proved to be crucial to the resulting ice load differences. Although we saw from Figure 4.20 that the warm run had more than 10% higher average LWC than the control in many high altitude grid points, more frequent melting episodes and periods with no icing caused the warm run to have considerably smaller averaged accumulated ice loads across the domain. Figure 5.2 showed that the added LWC can indeed lead to larger ice loads in the absence of extra melting- or no icing episodes, and similar experiments should be made for different winters in order to generalize the results found in this study. It is also possible that increasing the temperatures by a smaller  $\Delta T$  would limit the amount of extra melting episodes and still cause higher cloud LWC in high altitude regions, leading to more icing in the warm run. Additional simulations where e.g. the temperature is increased by only 1 °C should therefore also be performed. Improvements could also be made to our icing simulations by utilizing data from multiple vertical model levels. With the aid of higher resolution topographic maps, vertical interpolation could give a better representation of the real world icing conditions.



# Bibliography

- Allen, Myles R. and William J. Ingram (2002). "Constraints on future changes in climate and the hydrologic cycle". In: *Nature* 419.6903, pp. 224–232. ISSN: 0028-0836. DOI: [10.1038/nature01092](https://doi.org/10.1038/nature01092).
- Fikke, Svein M., Jón Egill Kristjánsson, and Bjørn Egil Kringlebotn Nygaard (2008). "Modern Meteorology and Atmospheric Icing". en. In: *Atmospheric Icing of Power Networks*. Ed. by Masoud Farzaneh. DOI: 10.1007/978-1-4020-8531-4\_1. Dordrecht: Springer Netherlands, pp. 1–29. ISBN: 978-1-4020-8530-7 978-1-4020-8531-4.
- Finstad, Karen J., Edward P. Lozowski, and Lasse Makkonen (1988). "On the Median Volume Diameter Approximation for Droplet Collision Efficiency". en. In: *Journal of the Atmospheric Sciences* 45.24, pp. 4008–4012. ISSN: 0022-4928, 1520-0469. DOI: [10.1175/1520-0469\(1988\)045<4008:OTMVDA>2.0.CO;2](https://doi.org/10.1175/1520-0469(1988)045<4008:OTMVDA>2.0.CO;2).
- García-Díez, M. et al. (2013). "Seasonal dependence of WRF model biases and sensitivity to PBL schemes over Europe". en. In: *Quarterly Journal of the Royal Meteorological Society* 139.671, pp. 501–514. ISSN: 00359009. DOI: [10.1002/qj.1976](https://doi.org/10.1002/qj.1976).
- Intergovernmental Panel on Climate Change, ed. (2014a). *Climate Change 2013 - The Physical Science Basis: Working Group I Contribution to the Fifth Assessment Report of the Intergovernmental Panel on Climate Change*. Cambridge: Cambridge University Press. ISBN: 978-1-107-41532-4.
- "Long-term Climate Change" (2014b). "Long-term Climate Change: Projections, Commitments and Irreversibility Pages 1029 to 1076". In: *Climate Change 2013 - The Physical Science Basis*. Ed. by Intergovernmental Panel on Climate Change. DOI: 10.1017/CBO9781107415324.024. Cambridge: Cambridge University Press, pp. 1029–1136. ISBN: 978-1-107-41532-4.
- Kringlebotn Nygaard, Bjørn Egil, Jón Egill Kristjánsson, and Lasse Makkonen (2011). "Prediction of In-Cloud Icing Conditions at Ground Level Using the WRF Model". en. In: *Journal of Applied Meteorology and Climatology* 50.12, pp. 2445–2459. ISSN: 1558-8424, 1558-8432. DOI: [10.1175/JAMC-D-11-054.1](https://doi.org/10.1175/JAMC-D-11-054.1).
- Lamb, Dennis and Johannes Verlinde (2011). *Physics and chemistry of clouds*. OCLC: ocn694393873. Cambridge ; New York: Cambridge University Press. ISBN: 978-0-521-89910-9.
- Lozowski, EP and L Makkonen (2005). "Fifty years of progress in modelling the accumulation of atmospheric ice on power network equipment". In:

- Proc. Eleventh International Workshop on Atmospheric Icing on Structures, Montreal, CD-ROM.*
- Makkonen, L. (2000). "Models for the growth of rime, glaze, icicles and wet snow on structures". en. In: *Philosophical Transactions of the Royal Society A: Mathematical, Physical and Engineering Sciences* 358.1776, pp. 2913–2939. ISSN: 1364-503X, 1471-2962. DOI: [10.1098/rsta.2000.0690](https://doi.org/10.1098/rsta.2000.0690).
- Makkonen, Lasse (1989). "Estimation of wet snow accretion on structures". en. In: *Cold Regions Science and Technology* 17.1, pp. 83–88. ISSN: 0165232X. DOI: [10.1016/S0165-232X\(89\)80018-7](https://doi.org/10.1016/S0165-232X(89)80018-7).
- Pavelsky, Tamlin M. et al. (2012). "Changes in orographic precipitation patterns caused by a shift from snow to rain: OROGRAPHIC PRECIPITATION PATTERNS". en. In: *Geophysical Research Letters* 39.18. ISSN: 00948276. DOI: [10.1029/2012GL052741](https://doi.org/10.1029/2012GL052741).
- Thompson, Gregory et al. (2008). "Explicit Forecasts of Winter Precipitation Using an Improved Bulk Microphysics Scheme. Part II: Implementation of a New Snow Parameterization". en. In: *Monthly Weather Review* 136.12, pp. 5095–5115. ISSN: 0027-0644, 1520-0493. DOI: [10.1175/2008MWR2387.1](https://doi.org/10.1175/2008MWR2387.1).
- Trenberth, Ke (2011). "Changes in precipitation with climate change". en. In: *Climate Research* 47.1, pp. 123–138. ISSN: 0936-577X, 1616-1572. DOI: [10.3354/cr00953](https://doi.org/10.3354/cr00953).
- Tveito, Ole Einar (2010). "An assessment of circulation type classifications for precipitation distribution in Norway". en. In: *Physics and Chemistry of the Earth, Parts A/B/C* 35.9-12, pp. 395–402. ISSN: 14747065. DOI: [10.1016/j.pce.2010.03.044](https://doi.org/10.1016/j.pce.2010.03.044).
- Zerr, Ryan J. (1997). "Freezing Rain: An Observational and Theoretical Study". en. In: *Journal of Applied Meteorology* 36.12, pp. 1647–1661. ISSN: 0894-8763, 1520-0450. DOI: [10.1175/1520-0450\(1997\)036<1647:FRAOAT>2.0.CO;2](https://doi.org/10.1175/1520-0450(1997)036<1647:FRAOAT>2.0.CO;2).